



## Molecular gas along the old radio jets of the cluster-central type 2 quasar IRAS 09104+4109

Ewan O'Sullivan, Francoise Combes, Arif Babul, Scott Chapman, Kedar A.  
Phadke, Gerrit Schellenberger, Philippe Salomé

### ► To cite this version:

Ewan O'Sullivan, Francoise Combes, Arif Babul, Scott Chapman, Kedar A. Phadke, et al.. Molecular gas along the old radio jets of the cluster-central type 2 quasar IRAS 09104+4109. Monthly Notices of the Royal Astronomical Society, 2021, 508 (3), pp.3796-3811. 10.1093/mnras/stab2825 . hal-03385268

**HAL Id: hal-03385268**

**<https://hal.science/hal-03385268>**

Submitted on 21 Apr 2023

**HAL** is a multi-disciplinary open access archive for the deposit and dissemination of scientific research documents, whether they are published or not. The documents may come from teaching and research institutions in France or abroad, or from public or private research centers.

L'archive ouverte pluridisciplinaire **HAL**, est destinée au dépôt et à la diffusion de documents scientifiques de niveau recherche, publiés ou non, émanant des établissements d'enseignement et de recherche français ou étrangers, des laboratoires publics ou privés.

# Molecular gas along the old radio jets of the cluster-central type 2 quasar IRAS 09104+4109

Ewan O’Sullivan<sup>1</sup>,<sup>★</sup> Françoise Combes,<sup>2,3</sup> Arif Babul,<sup>4</sup> Scott Chapman,<sup>5</sup> Kedar A. Phadke,<sup>6</sup> Gerrit Schellenberger<sup>1</sup> and Philippe Salomé<sup>2</sup>

<sup>1</sup>Center for Astrophysics | Harvard & Smithsonian, 60 Garden Street, Cambridge, MA 02138, USA

<sup>2</sup>LERMA, Observatoire de Paris, CNRS, PSL Univ., Sorbonne Univ., F-75014 Paris, France

<sup>3</sup>Collège de France, 11 place Marcelin Berthelot, F-75005 Paris, France

<sup>4</sup>Department of Physics and Astronomy, University of Victoria, Victoria, BC V8W 2Y2, Canada

<sup>5</sup>Department of Physics and Atmospheric Science, Dalhousie University, Halifax, NS B3H 3J5, Canada

<sup>6</sup>Department of Astronomy, University of Illinois, 1002 West Green Street, Urbana, IL 61801, USA

Accepted 2021 September 28. Received 2021 September 24; in original form 2021 July 8

## ABSTRACT

We present Northern Extended Millimeter Array (NOEMA) CO(2–1) maps of the  $z = 0.4418$  cluster-central quasi-stellar object (QSO) IRAS 09104+4109, which trace  $\sim 4.5 \times 10^{10} M_{\odot}$  of molecular gas in and around the galaxy. As in many low-redshift cool-core clusters, the molecular gas is located in a series of clumps extending along the old radio jets and lobes. It has a relatively low velocity dispersion [ $336^{+39}_{-35} \text{ km s}^{-1}$  full width at half-maximum (FWHM)] and shows no velocity gradients indicative of outflow or infall. Roughly half the gas is located in a central clump on the north-east side of the galaxy, overlapping a bright ionized gas filament and a spur of excess X-ray emission, suggesting that this is a location of rapid cooling. The molecular gas is unusually extended, out to  $\sim 55$  kpc radius, comparable to the scale of the filamentary nebula in the Perseus cluster, despite the much higher redshift of this system. The extent falls within the thermal instability radius of the intracluster medium (ICM), with  $t_{\text{cool}}/t_{\text{ff}} < 25$  and  $t_{\text{cool}}/t_{\text{eddy}} \sim 1$  within  $\sim 70$  kpc. Continuum measurements at 159.9 GHz from NOEMA and 850  $\mu\text{m}$  from the James Clerk Maxwell Telescope (JCMT) Submillimeter Common-User Bolometer Array 2 (SCUBA-2) show excess far-infrared emission, which we interpret as free–free emission arising from the ongoing starburst. These observations suggest that ICM cooling is not strongly affected by the buried QSO, and that cooling from the ICM can build gas reservoirs sufficient to fuel quasar-mode activity and drive the reorientation of the central active galactic nuclei (AGN).

**Key words:** galaxies: clusters: individual: CL 09104+4109 – galaxies: clusters: intracluster medium – galaxies: individual: IRAS 09104+4109 – quasars: general – X-rays: galaxies: clusters.

## 1 INTRODUCTION

It is now well established that heating by active galactic nuclei (AGN) plays the dominant role in balancing radiative cooling in the cores of relaxed galaxy clusters. In the nearby Universe, AGN in group- and cluster-dominant galaxies are almost always radio-mode systems, with numerous X-ray observations convincingly showing the connection between the radio jets and cavities inflated in the hot intracluster medium (ICM; see e.g. McNamara & Nulsen 2007; Fabian 2012; Gitti, Brighenti & McNamara 2012). The brightest cluster galaxies (BCGs) of cool-core clusters are often surrounded by extended filamentary optical emission-line nebulae (e.g. Fabian et al. 2003; Crawford, Sanders & Fabian 2005a; Crawford et al. 2005b; McDonald et al. 2010; McDonald, Veilleux & Mushotzky 2011; Lakhchaura et al. 2018), in many cases spatially correlated with molecular gas (e.g. Salomé et al. 2006, 2011; Russell et al. 2016, 2017a,b; Vantighem et al. 2016, 2017, 2018; Olivares et al. 2019), soft X-ray structures (e.g. Werner et al. 2014), and young

stars (e.g. Canning et al. 2014). These filamentary nebulae typically extend a few tens of kiloparsec (kpc) and can contain  $10^9$ – $10^{11} M_{\odot}$  of molecular gas.

The ionized and molecular gas is considered to be the product of cooling from the ICM, and the most likely fuel source for the AGN of the BCG. The nebulae tend to be found in systems where the central cooling time is short ( $< 1$  Gyr) and the ICM entropy is low ( $< 30 \text{ keV cm}^2$ ; Cavagnolo et al. 2008; Rafferty, McNamara & Nulsen 2008), and there is evidence that AGN jet power is correlated with the molecular gas mass (Babyk et al. 2019) and, tentatively, with the  $H\alpha$  emission from the ionized component (Lakhchaura et al. 2018). These correlations have been interpreted as indicating a threshold beyond which the ICM gas becomes thermally unstable and can potentially condense out (McCourt et al. 2012; Sharma et al. 2012; Gaspari, Ruszkowski & Oh 2013; Li & Bryan 2014a,b; Prasad, Sharma & Babul 2015).

However, there is still some debate as to whether the cooled material simply forms *in situ*, or whether some other factor is needed to trigger the condensation (McNamara et al. 2016; Hogan et al. 2017; Prasad, Sharma & Babul 2017, 2018; Voit et al. 2017; Gaspari et al. 2018; Qiu et al. 2020). The filaments of cooled gas are often

\* E-mail: [cosullivan@cfa.harvard.edu](mailto:cosullivan@cfa.harvard.edu)

found around the ICM cavities associated with radio lobes, or at smaller radii, in some cases lying along the presumed path of the lobes rise. This raises the possibility that as the lobes inflate and rise away from the AGN, they uplift cool ICM gas from the core (Revaz, Combes & Salomé 2008; Pope et al. 2010) that is either already thermally unstable or becomes so as it rises, and thus condenses out along the line of ascent (McNamara et al. 2016; Qiu et al. 2020). Uplift of ionized gas already present in the core may also be possible. Uplift of molecular gas would be more difficult given its high density, unless it is strongly connected to the ICM via surrounding layers of ionized gas (Li, Ruszkowski & Tremblay 2018) or magnetic fields (McCourt et al. 2015). Another possibility is that thermally unstable gas at larger radii is disturbed by the expansion of jets or lobes, with the induced turbulence and compression of the ICM triggering condensation (Gaspari et al. 2011; Gaspari, Ruszkowski & Sharma 2012; Li et al. 2015; Prasad et al. 2015, 2017).

While almost all nearby cluster-central AGN are low accretion rate, radiatively inefficient radio galaxies, at higher redshift many AGN are radiatively efficient quasar-type systems (e.g. Hlavacek-Larrondo et al. 2013) raising the question of how radiative cooling was regulated in clusters at earlier times. Unfortunately, very few low-redshift examples of cluster-central quasars are known. The BCG of the Phoenix Cluster hosts both a quasi-stellar object (QSO) and an extended filamentary nebula wrapped around two radio lobes (McDonald et al. 2019). The nebula contains  $\sim 2 \times 10^{10} M_{\odot}$  of molecular gas, fuelling star formation (SF) at the rate of  $500\text{--}800 M_{\odot} \text{ yr}^{-1}$ , but the AGN accretion rate is thought to be falling, causing a shift from quasar to jet-mode activity (Russell et al. 2017b; Prasad et al. 2020). A second cluster, H1812+643, hosts a type 1 (unobscured) quasar whose photon flux may be causing Compton cooling in the ICM (Russell et al. 2010; Reynolds et al. 2014; Walker et al. 2014). However, its fuel source is less clear; while the cooling flow should provide a plentiful supply of cooled ICM gas, there are conflicting reports of its molecular gas content (Aravena et al. 2011; Combes et al. 2011).

A third cluster-central quasar system is IRAS 09104+4109, a hyperluminous infrared galaxy (HyLIRG) located at the centre of the cluster CL 09104+4109 (also known as MACS J0913.7+4056). As well as hosting what may be the most luminous Compton-thick (type 2, obscured) QSO at  $z < 0.5$  (Farrah et al. 2016), the BCG has  $\sim 70$  kpc Fanaroff–Riley Class I (FR-I) radio jets whose radio spectrum suggests they were formed in a period of activity that ceased 120–160 Myr ago and a Very Long Baseline Array (VLBA) observation reveals a 200 pc scale inner radio double indicative of a more recent outburst, in the BCG nucleus (O’Sullivan et al. 2012, hereafter OS12). The QSO is obscured, but polarized optical emission traces its ionization cones, which are misaligned from the radio jets (Hines et al. 1999) indicating a change in orientation. IRAM 30-m CO(2–1) observations suggest the BCG contains  $3.2 \times 10^9 M_{\odot}$  of molecular gas, but only a relatively small amount of dust ( $< 5 \times 10^7 M_{\odot}$ ; Combes et al. 2011). The BCG appears to have undergone a burst of SF 70–200 Myr ago (Bildfell et al. 2008; Pipino et al. 2009) with a second burst, starting  $< 50$  Myr ago, producing a current star formation rate (SFR) of  $110^{+35}_{-28} M_{\odot} \text{ yr}^{-1}$  (Farrah et al. 2016). *Hubble Space Telescope* (HST) imaging reveals a number of ionized gas filaments around the BCG. Ground-based Integral Field Unit (IFU) observations of the brightest of these, a plume of [O III] emission extending  $\sim 27$  kpc from the BCG, show that its velocity is only  $\sim 100 \text{ km s}^{-1}$  offset from that of the galaxy (Crawford & Vanderriest 1996). Such small velocity offsets are typical of the filamentary nebulae seen in nearby cool-core clusters.

In this paper, we describe new Northern Extended Millimeter Array (NOEMA) and James Clerk Maxwell Telescope (JCMT) observations of IRAS 09104+4109, designed to probe the molecular gas and dust environment of the galaxy and determine where, and how much, gas is cooling out of the ICM to fuel the quasar. Throughout the paper we assume a flat cosmology with  $H_0 = 73 \text{ km s}^{-1} \text{ Mpc}^{-1}$ ,  $\Omega_{\Lambda} = 0.73$ , and  $\Omega_M = 0.27$ . We adopt a redshift of  $z = 0.4418$  for the galaxy, which gives an angular scale of  $1 \text{ arcsec} = 5.5 \text{ kpc}$ , luminosity distance  $D_L = 2372 \text{ Mpc}$ , and angular distance  $D_A = 1140 \text{ Mpc}$ , for ease of comparison with OS12.

## 2 OBSERVATIONS AND DATA REDUCTION

### 2.1 NOEMA

IRAS 09104+4109 was observed by the Northern Extended Millimeter Array (NOEMA) on 2018 November 29, 2019 December 29, and 2019 January 7 as program W18DB (PI: O’Sullivan). All 10 dishes were used, with the array in C configuration. We set the phase centre of the observations equal to the target coordinates,  $RA = 09^{\text{h}}:13^{\text{m}}:45^{\text{s}}.489$  and  $Dec. = 40^{\circ}:56':28''.22$ . We also adopted a tuning frequency of 159.9 GHz, which corresponds to the observer frame frequency of the redshifted CO(2–1) line, given the QSO redshift.

The baseline range was 24–368 m. The program was executed in good to typical winter weather conditions, with system temperature  $T_{\text{sys}} = 100\text{--}220 \text{ K}$  and a precipitable water vapour column between 2 and 7 mm. We used the PolyFix correlator that covers a total bandwidth of 15.5 GHz split between the lower and upper side band, covering the ranges between 142.5–150.2 and 157.8–165.5 GHz, respectively. The sources 0923+392, 0906+432, and 0916+390 were used as phase and amplitude calibrators, while 3C 84 and 3C 279 served as bandwidth and flux calibrators. We reduced the data using the CLIC package of the GILDAS software (Pety 2005; Gildas Team 2013). The final ( $u, v$ ) tables correspond to 6 h of total integration time, of which 4 h were on source.

We imaged the visibilities using the MAPPING software from GILDAS. At the tuning frequency of 159.9 GHz, the half-power primary beamwidth is 31.5 arcsec. We adopted natural weighting, yielding a synthesized beam of  $1.55 \text{ arcsec} \times 1.14 \text{ arcsec}$  with position angle (PA) =  $-16^{\circ}.7$ . We then rebinned the spectral axis at a resolution of  $30 \text{ km s}^{-1}$  ( $\sim 16 \text{ MHz}$  at 159.9 GHz). The resulting rms is  $0.72 \text{ mJy beam}^{-1}$ .

#### 2.1.1 NOEMA positional accuracy

The astrometry of the NOEMA data is expected to be highly accurate, but as a precaution, we confirmed it by imaging the continuum emission and comparing its centroid position with imaging from other wavelengths. OS12 present images of the system in a variety of bands, including *HST* and Canada–France–Hawaii Telescope optical data, *Chandra* X-ray images, Giant Metrewave Radio Telescope (GMRT), and Very Large Array (VLA) data in a total of six bands covering 240 MHz to 4.8 GHz, and a 1.4 GHz VLBA image. The 12 h VLBA observation (PI: Wrobel, project code BH0110) was phase referenced, performed in the nodding style (Wrobel et al. 2000), switching between alternate  $\sim 180$  s scans of the target and  $\sim 120$  s scans of the phase calibrator. It can therefore be expected to have milliarcsecond (mas) astrometric accuracy. The VLBA position was used for the phase centre of the NOEMA observation, and the position of the NOEMA continuum source agrees well with the

optical centroid of the galaxy, the central component of the megahertz (MHz) and gigahertz (GHz) radio emission, the hard X-ray source associated with the QSO, and the VLBA position. We are therefore confident in the astrometry of the NOEMA observation, and of the supporting data.

## 2.2 JCMT

IRAS 09104+4109 was observed with the Submillimeter Common-User Bolometer Array 2 (SCUBA-2) for a total of 6 h on source, in three programs from 2012 through 2018, the majority in our own program M15BL114 (PI: Chapman): M18BP056 – 30 min, M15BL114 – 5 h, M12AC15 – 30 min. Observations were conducted in Band 1–2 weather conditions ( $\tau_{225\text{ GHz}} \sim 0.04\text{--}0.08$ ). The mapping centre of the SCUBA-2 field was set to the same coordinates as the NOEMA phase centre. A standard 3 arcmin diameter DAISY mapping pattern was used (e.g. Kackley et al. 2010) that keeps the centre on one of the four SCUBA-2 subarrays at all times during the exposure.

The 12 individual 30 min scans were reduced using the dynamic iterative map-maker of the SMURF package (Chapin et al. 2013; Jenness et al. 2013). Maps from independent scans were co-added in an optimal stack using the variance of the data contributing to each pixel to weight spatially aligned pixels. Finally, since we are interested in (generally faint) extragalactic point sources, we applied a beam matched filter to improve point source detectability, resulting in a map that is convolved with an estimate of the 850 or 450  $\mu\text{m}$  beam.

The sky opacity at JCMT has been obtained by fitting extinction models to hundreds of standard calibrators observed since the commissioning of SCUBA-2 (Dempsey et al. 2012). These maps have been converted from pW to Jy using the standard conversion factors [Flux Conversion Factor (FCF)] of  $\text{FCF}_{450} = 491\text{ Jy beam}^{-1}\text{ pW}^{-1}$  and  $\text{FCF}_{850} = 547\text{ Jy beam}^{-1}\text{ pW}^{-1}$ , with effective 450 and 850  $\mu\text{m}$  beam sizes of 10 and 15 arcsec, respectively (Dempsey et al. 2013).

The variance map was derived for each pixel from the data time series (as in e.g. Koprowski 2015). The rms within the central 5 arcmin diameter region varies from 0.45 to 0.55 mJy beam $^{-1}$  at 850  $\mu\text{m}$  and 3.4 to 4.1 mJy beam $^{-1}$  at 450  $\mu\text{m}$ . Our depths reached at both 850 and 450  $\mu\text{m}$  and smaller beam sizes allow us to probe sources in the cluster core more effectively than the confusion-limited *Herschel* maps.

## 3 RESULTS

### 3.1 CO line emission

An initial examination of the continuum-subtracted NOEMA data cube suggests that most of the CO(2–1) flux is found within a few hundred km s $^{-1}$  of the BCG. A number of emission clumps are visible in this velocity range, close to the BCG or the radio jets.

When analysing data cubes containing spectral line emission, it is common to ‘clip’ the data, removing spectral channels where the signal falls below some significance threshold. As discussed in Dame (2011), while this reduces the noise level of the data, it also introduces biases, most notably a negative bias owing to the removal of spectral line wings and low-intensity extended emission. In many cases such a bias is acceptable, as it results in cleaner maps with well defined, highly significantly detected clouds. However, for fainter targets, excessive clipping can result in the loss of scientifically meaningful structures. Dame (2011) advocate an alternate approach in which the data are smoothed spatially and spectrally, and a clipped version of this smoothed cube is used as a mask. The smoothing suppresses

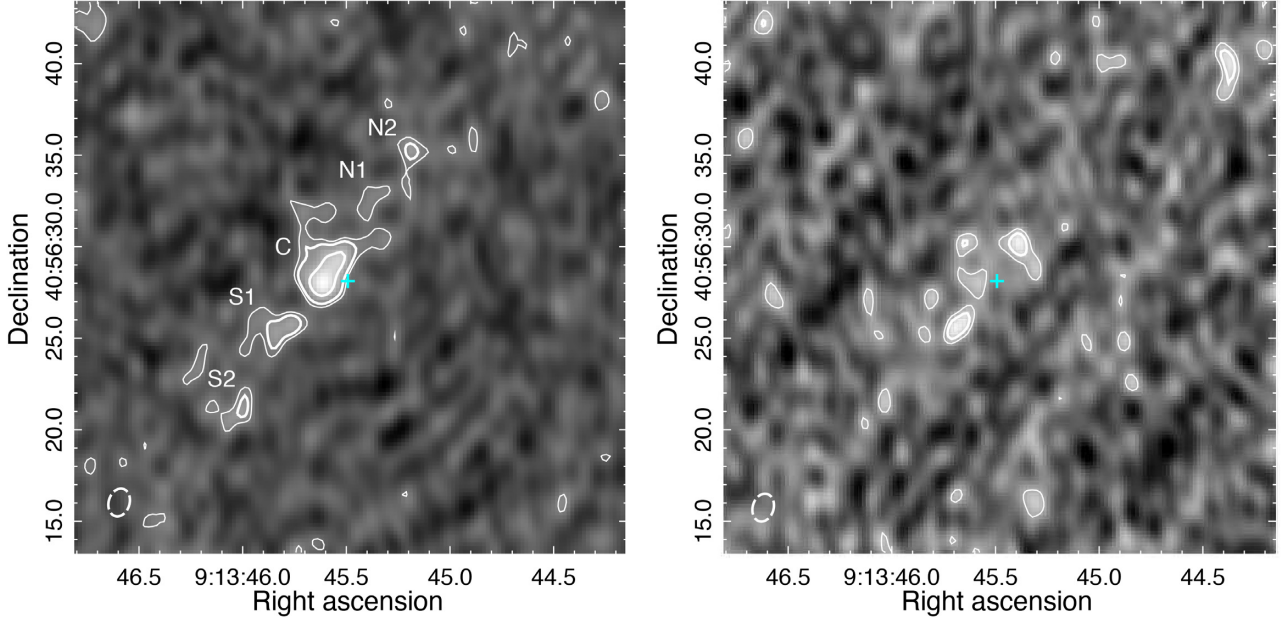
random noise peaks, while the significance of genuine emission, which can be expected to be in contiguous structures extending across multiple beams and/or spectral channels, should be enhanced. In creating images of our source, we experimented with this filtering method and with the choice of velocity range from which to extract data. We found that the best results were achieved using a mask Gaussian smoothed over two spectral channels and to  $\sim 3$  arcsec spatial resolution, which was then clipped to remove any region with  $< 2\sigma$  significant emission in an individual channel. Images were extracted in the velocity range  $-300$  to  $210\text{ km s}^{-1}$ . In the resulting image, several clumps of emission are detected at  $> 3\sigma$  significance, and we note that these are also detected at this significance level in images made with the unfiltered data.

Fig. 1 shows the resulting image, at the full spatial resolution of the observation (maps of the individual masked channels are shown in Fig. A1). The emission is dominated by a large clump near the middle of the image (clump C), whose centre is detected at  $> 6\sigma$  significance. Three smaller clumps (S1, S2, and N2) are detected at  $> 3\sigma$  significance along a line extending roughly north-west–south-east. Note that the images have not been corrected for the NOEMA primary beam [half-power beam width (HPBW) = 31.5 arcsec] so sensitivity declines toward the edge of the field of view. Contours mark the  $2\sigma$ ,  $3\sigma$ , and  $6\sigma$  significance levels; we have included the  $2\sigma$  contour to show the hints of more extended emission around the various clumps, and additional emission between them, but we note that we only consider  $3\sigma$  significant structures as detected in our analysis. Where  $2\sigma$  significant features are discussed, we emphasize that we cannot be sure that these are not noise features.

There is also a tentative detection of flux at  $\sim -1450\text{ km s}^{-1}$ . Fig. 1, right-hand panel, shows the flux map for the combination of two spectral channels,  $-1440$  and  $-1470\text{ km s}^{-1}$ . Two small clumps of emission are detected at  $> 3\sigma$  significance, positioned 2.5–3.5 arcsec (14–19 kpc) north-west and south-east of the BCG centroid. As expected for such a narrow velocity range, the image is relatively noisy, with numerous small clumps at  $> 2\sigma$  significance, and one other  $3\sigma$  significant region larger than the beam size, in the north-west corner of the image. Based on the noise level and image size, we expect 1–2 false  $3\sigma$  detections in the field.

We extracted spectra for the four clumps detected at  $> 3\sigma$  significance around the systemic velocity (C, N2, S1, and S2), for a region enclosing all of those clumps, and for a region enclosing the high-velocity clumps close to the BCG. Fig. 2 shows example spectra for clump C and for the large region enclosing the source as a whole. For the summed source, the spectrum is noisy, but a central peak is clear, and this is reasonably well approximated by a Gaussian centred close to the systemic velocity ( $+31 \pm 17\text{ km s}^{-1}$ ). The best-fitting model parameters are shown in Table 1. For clump C, the spectrum is more complex; the central peak has a tail extending to negative velocities, and a possible secondary spike corresponding to the high-velocity clumps is visible. We were able to model the spectrum using two Gaussian components for the main peak, and a narrow third Gaussian for the high-velocity component. With a small constant component to account for any remaining continuum flux (statistically consistent with zero), this provides a good fit to the data ( $\chi^2 = 129.18$  for 120 degrees of freedom). Imaging flux in the velocity range  $-750$  to  $-90\text{ km s}^{-1}$  suggests that the material forming the negative velocity tail is located primarily in the brightest peak of clump C, with some possible extension to the south-east toward clump S1. The material in the positive velocity peak is more widespread. The smaller clumps were all fitted using single Gaussians. Fit parameters for each clump are again shown in Table 1.





**Figure 1.** NOEMA moment 0 maps of integrated CO(2–1) flux, within  $-300$  to  $210 \text{ km s}^{-1}$  of the systemic velocity (left) and at  $-1440$  to  $-1470 \text{ km s}^{-1}$  (right). Contours mark levels  $2\sigma$ ,  $3\sigma$ , and  $6\sigma$  above the rms noise level ( $71.5 \text{ mJy beam}^{-1} \text{ km s}^{-1}$  for the left-hand panel,  $24.0 \text{ mJy beam}^{-1} \text{ km s}^{-1}$  for the right-hand panel). The dashed ellipse indicates the NOEMA beam, and the cross indicates the VLBA-determined position of the AGN. Note that the images have not been corrected for the NOEMA primary beam (HPBW =  $31.5 \text{ arcsec}$ ) so sensitivity declines toward the edge of the field.

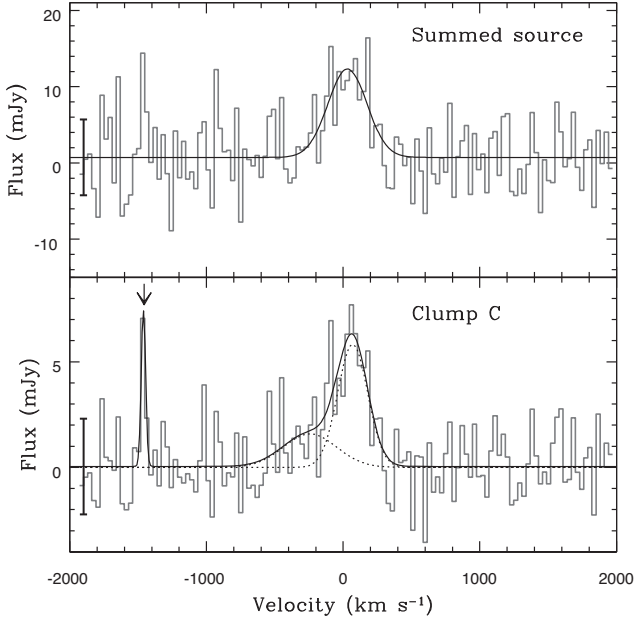


**Figure 2.** NOEMA spectra for the source as a whole (upper panel,  $4.97 \text{ mJy rms}$ ) and for clump C (lower panel,  $2.27 \text{ mJy rms}$ ) shown as grey histograms, with best-fitting models overlaid in solid black. For clump C, the two Gaussian components used to model the main peak are shown individually as dotted lines. An arrow marks the position of the high-velocity component. Error bars at  $-1950 \text{ km s}^{-1}$  indicate the rms noise level of each spectrum.

With the exception of clump C, all clumps have mean velocities consistent with the systemic velocity, and there is no clear trend in velocity along the line of clumps. The integrated flux in the spectrum for the source as a whole is marginally higher than the sum of the fluxes in the clumps, but consistent within the

**Table 1.** Best-fitting spectral model parameters and fluxes for the summed source and the component clumps.

Component	$\langle v \rangle$ ( $\text{km s}^{-1}$ )	Gaussian FWHM ( $\text{km s}^{-1}$ )	$S_{\text{CO}} \Delta v$ ( $\text{Jy km s}^{-1}$ )	$M_{\text{mol}}$ ( $10^{10} M_{\odot}$ )
Summed	$31 \pm 17$	$336^{+39}_{-35}$	$4.15^{+0.48}_{-0.45}$	$4.56^{+0.53}_{-0.49}$
C	$70^{+32}_{-42}$	$259^{+92}_{-77}$	$1.61^{+0.62}_{-0.75}$	$1.77^{+0.82}_{-0.68}$
N2	$-242^{+178}_{-250}$	$459^{+198}_{-339}$	$0.77^{+0.69}_{-0.57}$	$0.85^{+0.76}_{-0.63}$
S1	$44^{+108}_{-97}$	$320^{+174}_{-119}$	$0.15^{+0.09}_{-0.08}$	$0.16^{+0.10}_{-0.08}$
S2	$2 \pm 42$	$315^{+86}_{-68}$	$0.58^{+0.16}_{-0.15}$	$0.64^{+0.18}_{-0.16}$
HV	$8^{+64}_{-62}$	$278^{+119}_{-140}$	$0.27 \pm 0.12$	$0.30 \pm 0.13$
	$-1456^{+4}_{-5}$	$40^{+14}_{-31}$	$0.50^{+0.11}_{-0.09}$	$0.55^{+0.12}_{-0.10}$

uncertainties. Based on the integrated flux measured from these models, we estimate the molecular gas mass ( $M_{\text{mol}}$ ) in the source as a whole, and in each clump, following O’Sullivan et al. (2018) and adopting the conversion factor for nearby quiescent galaxies,  $\alpha_{\text{CO}} = 4.6$  (Solomon & Vanden Bout 2005). This suggests a total mass of molecular gas of  $\sim 4.5 \times 10^{10} M_{\odot}$  at the velocity of the BCG. However, we note that in ultraluminous infrared galaxies (ULIRGs) and intensely star-forming systems CO is expected to be more luminous than in quiescent galaxies, owing to higher densities and temperatures in the molecular clouds. These conditions may hold in IRAS 09104+4109, particularly in clump C. Combes et al. (2011) assumed  $\alpha_{\text{CO}} = 0.8$  for their molecular gas mass estimate of this system. Similarly, for their estimate of the CO mass in and around the BCG of the Phoenix Cluster, Russell et al. (2017b) assumed a lower conversion factor based on the work of Downes & Solomon (1998). If we adopted the  $\alpha_{\text{CO}} = 0.8$ , we would find a total molecular gas mass of  $\sim 7.9 \times 10^9 M_{\odot}$ , a factor of  $2.5\times$  greater than the IRAM 30-m mass estimate, but we note that we cannot be certain of the conditions in the gas with the available data.

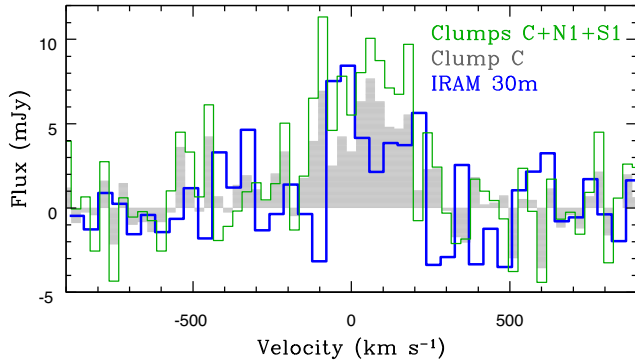


**Figure 3.** IRAM 30-m CO(2–1) spectrum (heavy blue line) plotted over the NOEMA CO(2–1) spectrum for clump C (shaded grey) and the summed spectrum of clumps C, N1, and S1 (thinner green line).

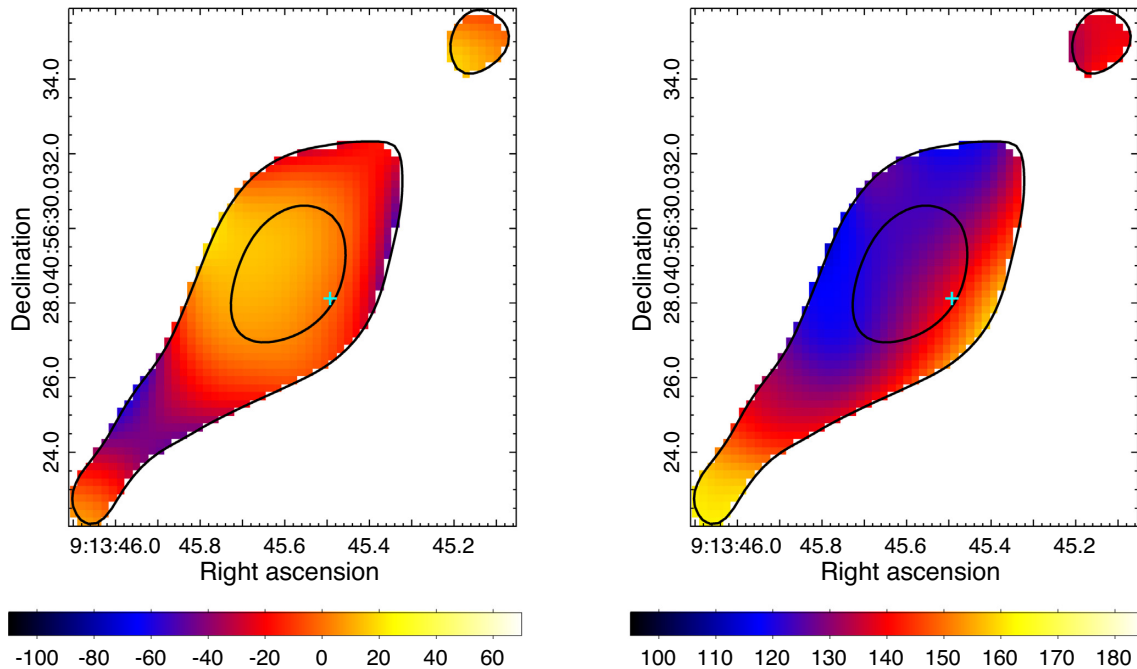
### 3.1.1 Comparison with IRAM 30-m detection

Fig. 3 shows a comparison of the IRAM 30-m spectrum for IRAS 09104+4109 (at slightly higher resolution than that presented by Combes et al. 2011) with the NOEMA spectrum of clump C and the summed spectrum of clumps C+N1+S1. Note that clump N1 is only  $2\sigma$  significant in our images, but as it falls well within the IRAM 30-m beam, we have included it to make sure any flux contribution from this region is included in the comparison. The IRAM 30-m spectrum appears to be double peaked, but when fitted with a single Gaussian is found to be relatively narrow ( $\text{FWHM} = 225 \pm 55 \text{ km s}^{-1}$ ) with a flux of  $1.4 \pm 0.4 \text{ Jy km s}^{-1}$ . The primary beam of the 30-m telescope has a HPBW of 15.4 arcsec at 159.9 GHz, roughly half the diameter of the NOEMA primary beam, so the older observation will not have included the outer clumps of emission we observe. Comparing the spectra, the overall line width in the IRAM 30-m spectrum is similar to that of clump C,

or clumps C+N1+S1, but the line height is more similar to that of clump C alone. Comparing the Gaussian fits to the lines, the flux and line width from the IRAM 30-m are similar to those of the dominant component of clump C ( $\text{FWHM} = 259^{+92}_{-77} \text{ km s}^{-1}$ ,  $1.61^{+0.62}_{-0.75} \text{ Jy km s}^{-1}$ ) and the mean velocities are comparable within the uncertainties ( $\langle v \rangle_{\text{IRAM}} = 32 \pm 30 \text{ km s}^{-1}$  compared to  $\langle v \rangle_{\text{clump C}} = 70^{+32}_{-42} \text{ km s}^{-1}$ ). It seems possible, therefore, that the shallower IRAM 30-m observation was dominated by emission from clump C. For comparison the total flux in clumps C+N1+S1 is  $\sim 3.28 \text{ Jy km s}^{-1}$ . Alternatively, the baseline continuum level of the IRAM 30-m data may have been overestimated, leading to the narrower line width and CO(2–1) flux underestimate. In either case, it seems clear that the NOEMA interferometer observations are recovering all of the flux detected by the IRAM 30-m and more.

### 3.1.2 CO velocity maps

At full resolution, maps of moments 1 and 2 (radial velocity and velocity dispersion) are very noisy, owing to the limited signal-to-noise ratio of the data in the individual clumps. We therefore created images from a broader velocity range ( $-420$  to  $360 \text{ km s}^{-1}$ ) smoothed with a 3 arcsec HPBW restoring beam, and applying the  $2\sigma$  clipping mask described above. We also reject all pixels whose flux level in the final moment 0 map is less than  $4\sigma$  significant. These images are shown in Fig. 4. At this resolution, a general north-west–south-east structure is visible, with the central clump (which now includes its immediate neighbours) detected at high ( $>8\sigma$ ) significance. A small clump is found to the north-west, corresponding to clump N2 in the full resolution image, while a tail extends to the south-east, its tip corresponding roughly with clump S2. The moment 1 map shows the relative velocity of the CO emission to be small compared to the BCG, generally  $<100 \text{ km s}^{-1}$ . The moment 2 map shows generally small velocity dispersion in the gas,  $\sim 110$ – $130 \text{ km s}^{-1}$ ,



**Figure 4.** Maps of smoothed NOEMA CO(2–1) moment 1 (velocity relative to the BCG, in  $\text{km s}^{-1}$ ) and moment 2 (velocity dispersion, in  $\text{km s}^{-1}$ ) made using a 3 arcsec HPBW restoring beam. Both panels show the same field of view. Contours indicate flux  $4\sigma$  and  $8\sigma$  above the smoothed rms noise level. The cross indicates the VLBA-determined AGN position.

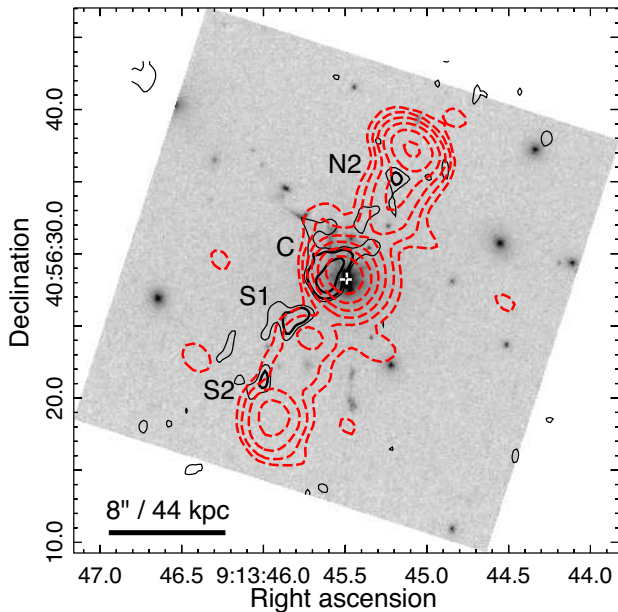


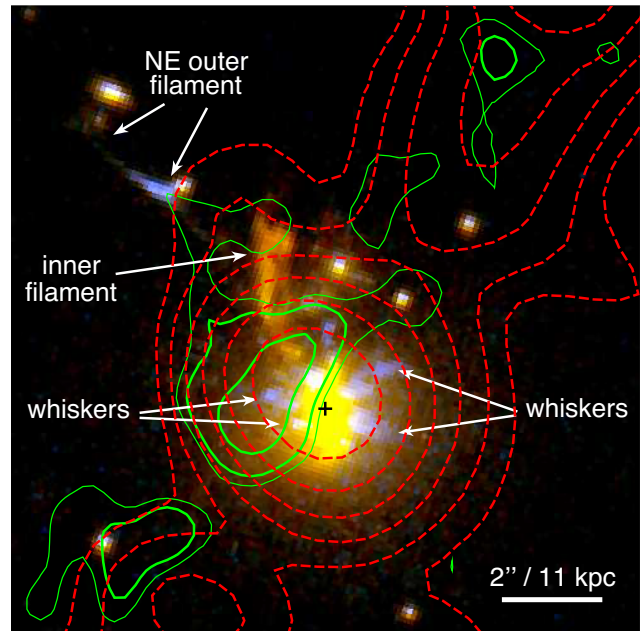
**Figure 5.** *HST* F622W image of IRAS 09104+4109 overlaid with NOEMA CO(2–1) contours (black, levels as in Fig. 1) and GMRT 1.28 GHz contours (dashed red, from OS12) starting at  $3 \times \text{rms}$  and increasing in steps of factor 2, with  $\text{rms} = 20 \mu\text{Jy beam}^{-1}$ . The cross indicates the position of the AGN.

except on the western side of the main clump and in the south-east tail, where values  $\sim 160 \text{ km s}^{-1}$  are found. In the region overlapping the BCG centroid it is possible that the higher velocity dispersions are associated with the gas in the deepest parts of the potential well of the BCG.

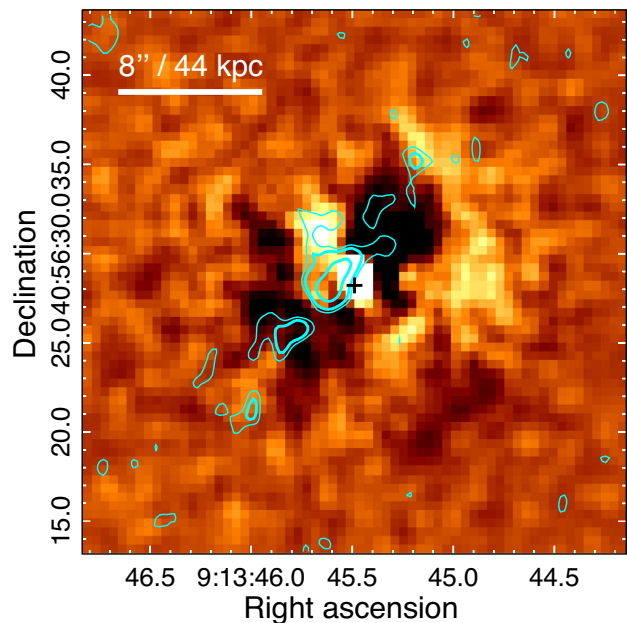
### 3.1.3 Comparison with radio continuum, X-ray, and optical structures

Fig. 5 shows the contours of the low-velocity CO(2–1) emission overlaid on an *HST* F622W image of the cluster core, with GMRT 1.28 GHz radio continuum contours showing emission from the old radio jets and lobes associated with the BCG. Further description of the *HST* and GMRT data used in this section can be found in OS12. The majority of the CO emission, including clumps C, S1, and S2, falls along the east side of the radio jets. Clump N2 is located at the base of the northern radio lobe, while clump S2 is located on the eastern side of the base of the south radio lobe. It is notable that clump C only overlaps the eastern half of the BCG.

Fig. 6 shows the relationship of the BCG and CO clumps in greater detail. Clump C overlaps the base of the brightest of the optical filaments associated with the galaxy (the ‘inner filament’) and some of the smaller filaments extending out of the BCG (‘whiskers’). As mentioned in Section 1, the [O III] emission from the inner filament has a velocity of  $\sim 100 \text{ km s}^{-1}$  relative to the BCG, comparable to the velocity of the molecular gas. It therefore seems plausible that the two are cospatial, though the CO appears more extended than the ionized gas. At the  $2\sigma$  significance level, there is a suggestion of an extension north-east from clump C, in a similar direction to that of the inner filament and north-east optical filament. This would be interesting if real, but the low significance makes any association speculative. Deeper *HST* observations and NOEMA observations would perhaps give a clearer view of the connection between the two gas phases.



**Figure 6.** False colour *HST* PC2 image of IRAS 09104+4109, zoomed in to show the optical filaments north-east of the BCG. An 814W filter image is used for the red band, a 622W image for green band, and a scaled 622W subtracted from the 814W image for the blue band. This combination is chosen to emphasize the optical filaments referred to in the text. NOEMA CO(2–1) (green) and GMRT 1.28 GHz contours (dashed red, from OS12) are overlaid. The cross indicates the position of the AGN.



**Figure 7.** *Chandra* 0.3–3 keV residual image, smoothed with a 2-pixel ( $\sim 1 \text{ arcsec}$ ) Gaussian, with NOEMA CO(2–1) contours (cyan, levels as in Fig. 1) overlaid. The cross indicates the position of the AGN.

Fig. 7 shows the CO contours overlaid on a lightly smoothed *Chandra* 0.3–3 keV residual map, after subtraction of the best-fitting elliptical  $\beta$ -model (see OS12 for details, and their fig. 7 for a comparison with the GMRT radio contours). The dark regions north-west and south-east of the AGN are interpreted as cavities



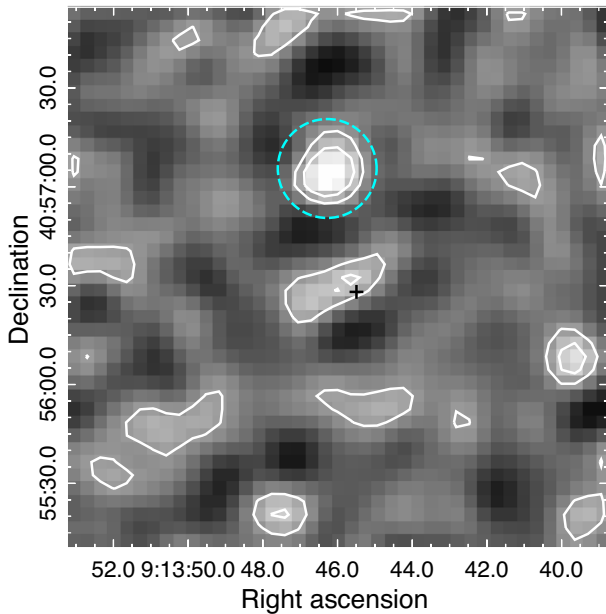


**Figure 8.** JCMT SCUBA-2 850  $\mu\text{m}$  map of the region around IRAS 09104+4109, whose position is marked by a cross. Contours levels are 2 and 3 times the noise level,  $0.74 \text{ mJy beam}^{-1}$ . The circle indicates the effective size of the SCUBA-2 beam (14.6 arcsec FWHM) and is centred on the nearby source mentioned in the text.

inflated by the old radio jets. They only extend along the jets and are not correlated with the radio lobes, but as discussed in OS12 the *Chandra* exposure may be insufficient to detect cavities on the scale of the lobes, which are relatively small. Clump S1 falls within the southern cavity and N2 is at the outer edge of the northern cavity. Clump N2 falls on a linear X-ray surface brightness excess structure, while clump C partly overlaps another region of excess X-ray emission extending north-east from the BCG, corresponding to the inner optical filament. The linear structure close to clump N2 could be gas compressed by the expansion of the cavity, or could be associated with sloshing motions. The brighter structure overlapping clump C seems more likely to be a region of rapid cooling; this would explain the apparent spatial correlation between X-ray, [O III], and CO emission.

### 3.2 Continuum emission

Continuum emission is detected from IRAS 09104+4109 in both the NOEMA and JCMT SCUBA-2 data, with 159.9 GHz and 850  $\mu\text{m}$  flux densities of  $0.56 \pm 0.03 \text{ mJy}$  and  $3.355 \pm 0.7 \text{ mJy}$ , respectively. Fig. 8 shows a section of the SCUBA2 map centred on the galaxy. IRAS 09104+4109 is among the weaker sources in the 850  $\mu\text{m}$  map, with a brighter source centred close to WISEA J091346.94+405703.1, only  $\sim 38$  arcsec to the north. The peak of the 850  $\mu\text{m}$  flux is located slightly to the north-east of the nucleus of IRAS 09104+4109, but given the size of the SCUBA-2 beam (14.6 arcsec FWHM), the position is reasonably consistent with that of the galaxy.

We have also reanalysed the *Herschel* Spectral and Photometric Imaging Receiver (SPIRE) data for the system, and the resulting 250, 350, and 500  $\mu\text{m}$  images are shown in Fig. 9. At 250  $\mu\text{m}$  IRAS 09104+4109 is relatively bright, while the 850  $\mu\text{m}$  source to its north is considerably weaker. However, at longer wavelengths the

HyLIRG becomes fainter, and the instrument resolution poorer, so that while at 350  $\mu\text{m}$  the two sources can still be separated, at 500  $\mu\text{m}$  only the northern source is visible. Table 2 lists the fluxes and upper limits measured from the NOEMA, SCUBA-2, and SPIRE.

Farrah et al. (2016) explored the infrared spectrum of IRAS 09104+4109, describing it with two radiative transfer grid models, the first (dominant at shorter wavelengths) an AGN whose radiation is reprocessed by surrounding dust (Efstathiou & Rowan-Robinson 1995; Efstathiou et al. 2013) and the second a dusty starburst (Efstathiou, Rowan-Robinson & Siebenmorgen 2000, dominant in the far-infrared). The combination of the two components modelled the infrared emission well (see their fig. 1), but at wavelengths longer than 250  $\mu\text{m}$  only upper limits on the flux were available, and the model was thus unconstrained. In the radio, OS12 found the 151 MHz–15 GHz spectrum to be well described by a power law with spectral index<sup>1</sup>  $\alpha = 1.25 \pm 0.01$ .

Fig. 10 shows the infrared to radio spectrum of IRAS 09104+4109, including our continuum flux measurements. Our 159.9 GHz NOEMA and 850  $\mu\text{m}$  SCUBA-2 continuum measurements clearly belong to the infrared part of the spectrum but comparison with Farrah et al. (2016) shows that they fall above the flux expected from their starburst model.

We modelled the spectrum using the Code Investigating GALaxy Emission (CIGALE; Boquien et al. 2019). In addition to the starburst and AGN radiative components used by Farrah et al. (2016), we included nebular emission from star-forming regions, and a power law to describe the synchrotron emission from the radio jets. A delayed  $\tau$  star formation history (SFH) was used with a recent burst (10–50 Myr) accounting for the star-forming population. The Bruzual & Charlot (2003) stellar population library was adopted, assuming a Chabrier (2003) initial mass function (IMF). The metallicity was allowed to vary from  $10^{-4}$  to  $5 \times 10^{-2}$ , where  $2 \times 10^{-2}$  corresponds to the solar value. The reprocessed dust emission associated with the SF was modelled using the templates of Dale et al. (2014), which are based on a sample of star-forming nearby galaxies, and parametrized by a single parameter  $\eta$ , defined as  $dM_d(U) \propto U^{-\eta} dU$ , where  $M_d$  is the dust mass and  $U$  is the radiation field intensity. This component successfully fits the cold dust emission as seen in Fig. 10.

The SKIRTOR (Stalevski et al. 2016) library for dusty AGN tori, based on 3D Monte Carlo radiative transfer calculations, was used to model the infrared emission from the AGN heated dust. The synchrotron emission was modelled by a power law whose slope was allowed to vary in the range 1.0–1.5. The current version of CIGALE only fits to a maximum wavelength of 1 m, so the two longest wavelength radio fluxes are not included in the fit, but appear reasonably well described by the model anyway. The nebular emission component, representing free-free emission from star forming H II regions, was modelled using templates based on Inoue (2011), which were generated using models from the CLOUDY spectral synthesis code (Ferland et al. 1998). This component makes a significant contribution at millimetre to centimetre wavelengths, most notably affecting the fit to the 15 and 159 GHz data points. In total, the model has 12 free parameters, and the best fit has  $\chi^2 = 15.67$ .

Based on the model fit, the starburst age is  $25 \pm 13$  Myr, consistent with the upper limit of 50 Myr found by Farrah et al. (2016). The best-fitting synchrotron power-law spectral index is  $1.35 \pm 0.06$ , a little steeper than that found from the radio alone. The total

<sup>1</sup>The radio spectral index  $\alpha$  is defined as  $S_\nu \propto \nu^{-\alpha}$ , where  $S_\nu$  is the flux density at frequency  $\nu$ .



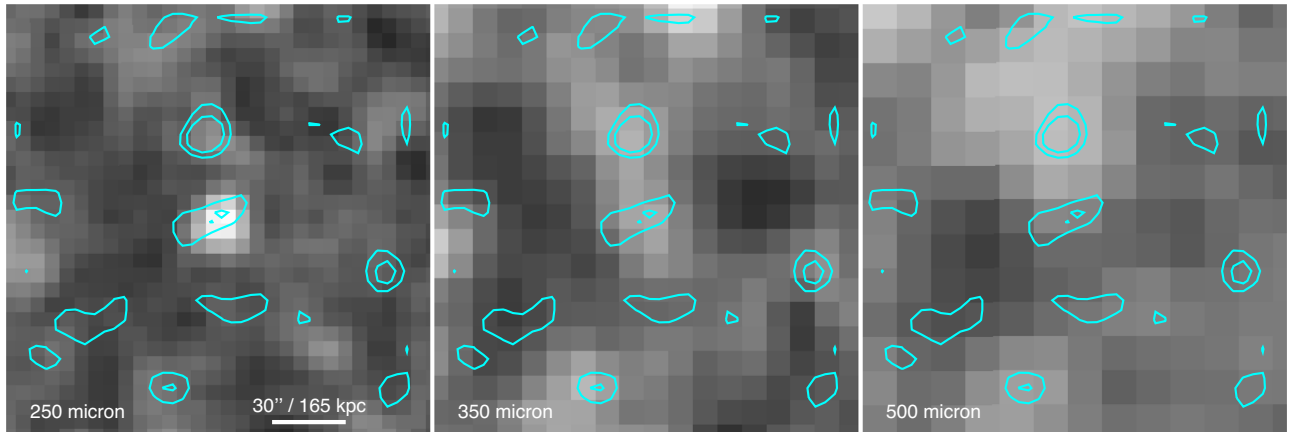


**Figure 9.** *Herschel* SPIRE 250, 350, and 500  $\mu\text{m}$  images centred on IRAS 09104 + 4109, with SCUBA-2 850  $\mu\text{m}$  contours overlaid. Contours levels are 2 and 3 times the noise level,  $0.74 \text{ mJy beam}^{-1}$ .

**Table 2.** Measured far-infrared, submillimetre, and millimetre-wave flux densities for IRAS 09104+4109 from NOEMA, JCMT SCUBA-2, and *Herschel* SPIRE. The wavelength for the NOEMA measurement corresponds to a frequency of 159.9 GHz.

Instrument	Wavelength ( $\mu\text{m}$ )	Flux density (mJy)
NOEMA	1875	$0.56 \pm 0.03$
SCUBA-2	850	$3.2 \pm 0.9$
	450	$<17.4$
SPIRE	500	$<24$
	350	$15.7 \pm 5.3$
	250	$53.3 \pm 4.1$

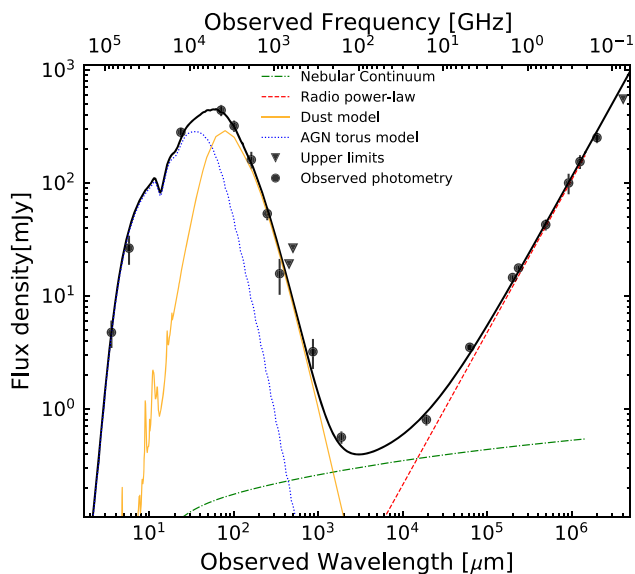


**Figure 10.** Spectrum of the continuum emission from the BCG from the infrared into the radio. Measured fluxes and uncertainties are marked by circles with error bars, inverted triangles indicate upper limits. The thick solid black line shows the fitted model, with the thinner lines indicating the AGN torus (blue dotted), dusty SF (orange solid), nebular continuum (green dot-dashed), and radio continuum (red dashed) components.

intrinsic infrared luminosity of the AGN radiative component is found to be  $[4.60 \pm 0.62] \times 10^{46} \text{ erg s}^{-1}$ , consistent with the value  $\sim 4.9 \times 10^{46} \text{ erg s}^{-1}$  found by Farrah et al. (2016). The half-opening angle of the AGN torus model is  $40^\circ$ , and an edge-on geometry is favoured, but we note that the combined infrared and X-ray modelling of Farrah et al. (2016) is likely to give a more reliable estimate of these geometric parameters than our fit.

## 4 DISCUSSION

### 4.1 ICM properties and molecular gas location

In general terms, the overall structure of the molecular gas is very similar to that observed in other cool-core galaxy clusters with central FR-I radio galaxies. Typically, a large fraction of the gas is found in or near the BCG, with the remainder in filaments, some of which may wrap around or fall behind the radio lobes and cavities, all at low velocities relative to the galaxy (see e.g. Olivares et al. 2019; Russell et al. 2019). In our case, clump C contains  $\sim 55$  per cent of the molecular gas, and all of the clumps (except the high-velocity component) have peak velocities within  $100 \text{ km s}^{-1}$  of the BCG. However, the molecular gas distribution around IRAS 09104+4109 is significantly more extended than is usual. Olivares et al. (2019) find that for 13 clusters with extended molecular gas filaments, the largest extend  $\leq 25 \text{ kpc}$ . For comparison with another QSO-hosting cluster, the molecular filaments in the Phoenix Cluster extend  $\sim 20 \text{ kpc}$  (Russell et al. 2017b). Clump C extends  $\sim 3 \text{ arcsec}$  (16.5 kpc), while the smaller clumps extend out to  $\sim 55 \text{ kpc}$ . This is similar to the extent of the H $\alpha$  filamentary nebula complex around NGC 1275 (the BCG of the Perseus cluster; see e.g. Conselice, Gallagher & Wyse 2001; Gendron-Marsolais et al. 2018), many of whose filaments contain molecular gas (Salomé et al. 2006, 2011). However, NGC 1275 is the closest example of such a filamentary nebula, and is thus observed in greater depth than any other. The fact that we see a similar extent in IRAS 09104+4109 at  $z = 0.44$  emphasizes the unusual scale of its molecular gas complex.

The cluster has a strong cool core; OS12 report ICM entropy in the central 5 arcsec of  $\sim 20 \text{ keV cm}^2$ , and isobaric cooling time  $\sim 1 \text{ Gyr}$ . These values are derived from a deprojected spectral profile with limited resolution, but we can estimate values closer to the core, at least roughly. OS12 found a projected temperature in a 1.5–2.5 arcsec bin, immediately outside the region affected by the QSO, of  $3.27^{+0.31}_{-0.24} \text{ keV}$ . We fitted a  $\beta$ -model to the 0.5–7 keV surface

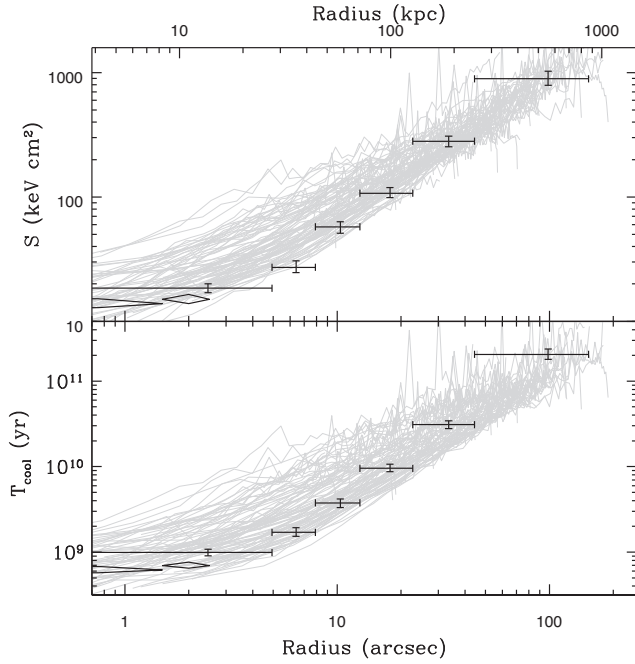


**Figure 11.** Profiles of entropy and isobaric cooling time for the cluster. Crossed error bars show the deprojected profiles from OS12. Grey lines show profiles of low-redshift strong cool-core clusters drawn from the ACCEPT sample of Cavagnolo et al. (2010). The diamonds show the entropy and cooling time estimated for the 1.5–2.5 arcsec ( $\sim 8$ –14 kpc) annulus based on the projected temperature and surface brightness profile.

brightness profile, excluding a 1.5 arcsec radius region centred on the AGN and regions covering the jets, lobes, and cavities. We find the best-fitting model has a core radius of  $r_c = 4.93^{+0.12}_{-0.14}$  arcsec and slope parameter  $\beta = 0.593 \pm 0.003$ . Normalizing a three-dimensional  $\beta$ -model with these parameters to match the density OS12 found in the central 5 arcsec, we estimate the central density to be  $n_e \sim 0.117 \text{ cm}^{-3}$ . Conservatively assuming that the temperature measured in the 1.5–2.5 arcsec bin also applies within 1.5 arcsec, we estimate the entropy in the central 1.5 arcsec (8.3 kpc) to be  $\sim 14 \text{ keV cm}^2$  and the isobaric cooling time in this region to be  $\sim 620 \text{ Myr}$ . In reality, the true value of the temperature, and thus the entropy and cooling time, is likely to be somewhat lower. Fig. 11 shows these estimates plotted against the deprojected entropy and cooling time profiles from OS12, and profiles for strong cool-core (SCC) clusters drawn from the sample of Cavagnolo et al. (2010); the cluster appears to have similar properties to the most strongly cooling SCC clusters at low redshift.

By comparison, the Phoenix Cluster has an entropy profile steeper than typical for the ACCEPT sample between  $\sim 30$  and 100 kpc, falls below any of the ACCEPT clusters inside  $\sim 30$ –40 kpc, and drops significantly inside  $\sim 0.007 R_{200}$  owing to a sharp decline in the inner temperature profile (McDonald et al. 2015; Prasad et al. 2020). The entropy profile for IRAS 09104+4109 flattens in the centre, but it should be noted that the Phoenix Cluster is a significantly more massive system ( $M_{200} \simeq 2 \times 10^{15} M_\odot$ , compared to  $6 \times 10^{14} M_\odot$  for CL 09104+4109; OS12). Scaled by mass, a similar central entropy dip would only have an extent of  $\sim 11.5 \text{ kpc}$  ( $\sim 2 \text{ arcsec}$ ) in our cluster, too small to be detected with the available *Chandra* data.

The ratio of the cooling time to the free-fall time has been widely used as an indicator of thermal instability in the ICM, with the extent of filamentary nebulae generally matching the radius at which

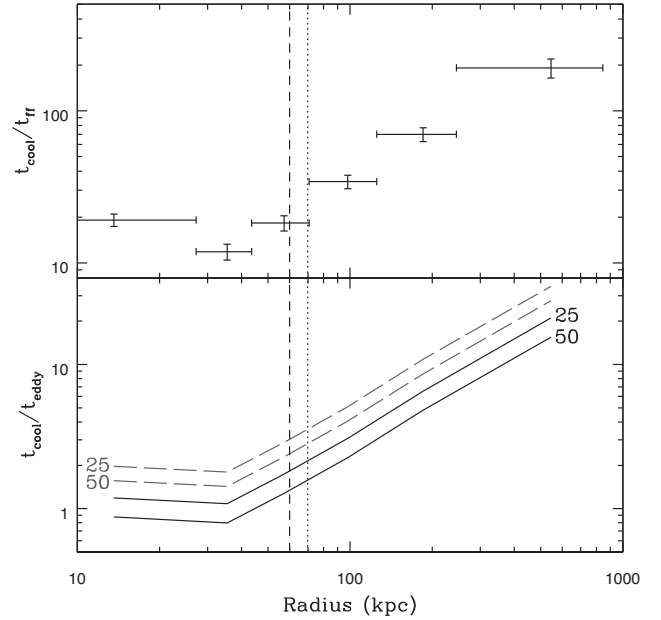


**Figure 12.** Profiles of the ratio of isochoric cooling time to free-fall time (upper panel) and eddy time (lower panel) in the ICM.  $t_{\text{cool}}/t_{\text{eddy}}$  profiles are labelled with the injection length scale ( $L$ , in kpc) used in the calculation. Black solid lines are for turbulent velocity dispersion  $\sigma_{v,L} = 190 \text{ km s}^{-1}$  and long-dashed grey lines for  $\sigma_{v,L} = 340 \text{ km s}^{-1}$ . The vertical dashed and dotted lines indicate the radial extent of the CO and old radio jets, respectively.

$t_{\text{cool}}/t_{\text{ff}} \lesssim 20$  (Voit et al. 2018). Based on the modelled mass profile of the cluster (see OS12) we can estimate the free-fall time at a given radius as

$$t_{\text{ff}} = \sqrt{\frac{2r}{g(r)}}, \quad (1)$$

where  $g(r)$  is the gravitational acceleration caused by the mass contained within radius  $r$ . Noting that OS12 calculated the isobaric cooling time, a factor of 5/3 longer than the isochoric cooling time that is generally used for comparison with the free-fall time, Fig. 12 shows the profile of  $t_{\text{cool}}/t_{\text{ff}}$  for the cluster. We find that  $t_{\text{cool}}/t_{\text{ff}} < 20$  out to at least  $\sim 60 \text{ kpc}$ . This agrees well with the extent of the CO clumps.

Gaspari et al. (2018) argue that the ratio of  $t_{\text{cool}}$  to the eddy turnover time-scale provides a more accurate indicator of thermal instability. As shown by Prasad et al. (2017), gas is expected to preferentially condense self-consistently in high density fluctuations caused by the turbulence injected as AGN jets or rising cavities disturb the ICM. Such condensation is expected where the ratio of cooling to eddy time-scales approaches unity. The eddy turnover time-scale is defined as

$$t_{\text{eddy}} = 2\pi \frac{r^{2/3} L^{1/3}}{\sigma_{v,L}}, \quad (2)$$

where  $\sigma_{v,L}$  is the velocity dispersion of the turbulence injected on length scale  $L$ . Neither of these parameters is directly observable with current instruments. However,  $L$  is likely to be comparable to the size of the radio jets or cavities. The turbulent velocities in the condensation regions is likely to drive turbulence in the gas that cools from them, therefore the velocity dispersion of the CO may be a proxy for the ICM. Converting the line-of-sight velocity dispersions measured in clump C to a three-dimensional velocity dispersion suggests that  $\sigma_{v,L}$  may be in the range  $190$ – $340 \text{ km s}^{-1}$ .

We estimate  $t_{\text{eddy}}$  for  $\sigma_{v,L} = 190$  and  $340 \text{ km s}^{-1}$  and  $L = 25$  or  $50 \text{ kpc}$ , scales chosen to match the size of the detected cavities or the extent of the CO emission. Fig. 12 shows the resulting profiles. We find that  $t_{\text{cool}}/t_{\text{eddy}}$  is close to unity throughout the region where CO is observed, supporting the idea that the ICM is thermally unstable and rapidly cooling out to at least  $60 \text{ kpc}$ .

## 4.2 Origin of the molecular gas

As mentioned in Section 1, the location at which gas cools out of the ICM and the mechanisms involved in producing molecular and ionized gas filaments in cluster cores are still subjects of debate. It has been suggested that the gas may condense out close to the cluster core and then be uplifted by rising radio lobes, that cool ICM gas is uplifted by the lobes and then condenses out along their line of expansion, or that the jets and lobes disturb thermally unstable gas at larger radii, which condenses *in situ*. For cluster-central quasars there is the additional possibility of ejection of cold gas from the BCG by a radiation-driven outflow.

Considering the last of these options first, many examples of high-velocity molecular outflows from quasars have been observed and although most are on sub-kpc scales (e.g. Ciccone et al. 2014; Fluetsch et al. 2019), there are examples where molecular clumps have been observed at distances of up to  $25\text{--}30 \text{ kpc}$  and velocities of  $1000\text{--}1700 \text{ km s}^{-1}$  relative to their AGN (Ciccone et al. 2015; Bischetti et al. 2019; Chartas et al. 2020). Optical spectroscopy of IRAS 09104+4109 has shown a  $\sim 1000 \text{ km s}^{-1}$  blueshifted component in some of the narrow emission lines of the AGN (e.g. Kleinmann et al. 1988; Crawford & Vanderriest 1996; Tran, Cohen & Villar-Martin 2000). However, the location of this quasar in the centre of a massive galaxy cluster means that such an outflow can be effectively ruled out. Any radiation-driven wind capable of ejecting molecular clouds out to a radius of  $55 \text{ kpc}$  would have a dramatic impact on the ICM. The molecular gas would be embedded in much larger plumes of hot gas that would disturb the structure of the ICM and themselves produce X-ray emission. We would expect OS12 to have seen any such plumes in the *Chandra* images and temperature map. As will be discussed later, we also have evidence that the QSO is misaligned with the radio jets, and we believe that the shut down of the jets occurred because the AGN accretion rate increased, causing it to enter its current quasar state. If that is correct, the CO cannot have been transported to its current location by a QSO outflow, since that outflow would have started after the radio jets shut down, and would not be correlated with them.

The distribution of the CO clumps along the old radio jets is generally consistent with scenarios involving uplift of ICM or molecular gas, or with disturbance of thermally unstable gas by the expanding jets. The close correlation of clumps S1 and S2 with the edges of the jets and lobes (see Fig. 5) is perhaps most consistent with the disturbance scenario. However, the clumps are not clearly correlated with the X-ray structures, as might be expected if they had formed from the coolest, highest density, or most compressed ICM gas. Clump N2 is located close to the bright linear filament on the northern boundary of the north cavity, but no clumps are found in the rest of the bright partial rim.

The amount of gas that can be uplifted by a buoyantly rising cavity is in principle equal to the mass of gas the cavity displaces, though simulations suggest that in practice only about half the mass can be lifted. Pope et al. (2010) describe three mechanisms of uplift: entrainment within rising lobes (probably not relevant in our case), upward drift of gas initially pushed aside by a rising lobe, and wake transport, in which a volume of gas immediately behind the lobe is

drawn up with it as it rises, potentially leaving a trail of material along its path. The position of clump N2 comes closest to what we might expect from wake transport.

Estimating the mass of gas displaced by the detected cavities along the jets, and for cavities with the size and position of the radio lobes, we find that the lobes could uplift  $\sim 4.3 \times 10^9 M_{\odot}$  of gas each. This is sufficient to lift clump N2, but less than the summed mass of clumps S1–S2. The detected cavities along the jets are capable of uplifting  $\sim 2\text{--}5 \times 10^{10} M_{\odot}$ . This would be sufficient to uplift clump S1 and perhaps some fraction of clump C, leaving the cavities in the lobes to uplift clumps S2 and N2. It is therefore at least plausible for the molecular gas to have formed from uplifted material, if there are sizable cavities coincident with the radio lobes. However, it should be noted that the mass of molecular gas we observe would be only a small fraction of the material that would have to be uplifted. For molecular gas to be uplifted it would have to be embedded within, and linked to, a much larger volume of less dense material, whose mass would also have to be lifted. If cool ICM gas was uplifted instead, we would expect only a small fraction to cool out and condense. The plausibility of uplift as an origin for the molecular gas is therefore a question of how much additional low-density material is needed to transport or produce the observed molecular gas.

*In situ* formation avoids the issues associated with uplift, but has other potential problems, in particular the question of the dust content of the cooling filaments. Filamentary cooling nebulae are observed to contain dust (e.g. Temi et al. 2018; Fogarty et al. 2019), and dust plays a critical role as a catalyst in the formation of molecular gas (e.g. Gould & Salpeter 1963; Hollenbach & Salpeter 1971), but unshielded dust grains in the ICM are likely to be rapidly destroyed via sputtering. Dust sources are present in the cluster core, e.g. supernovae and stellar mass loss from stars in the outer halo of the BCG, interstellar medium (ISM) stripped from infalling galaxies. Dust from such sources would need to remain shielded over long periods so as to be available when cooling and condensation was triggered. One possibility is that the combination of shielding by magnetic fields and efficient radiation of heat via molecular line emission could allow packets of dusty cooler gas to survive in the ICM. A comparison can be drawn with the highly multiphase shock region of the galaxy group Stephan’s Quintet (HCG 92). In that system, strong collisional shock heating failed to destroy all the molecular gas and dust in an H I filament tidally stripped from a spiral galaxy (Sulentic et al. 2001), and molecular clouds appear to be able to survive and grow (Guillard et al. 2009) despite being surrounded by a  $\sim 0.6 \text{ keV}$  thermal plasma (O’Sullivan et al. 2009). However, the time-scales over which such cool material can survive in the hotter ICM is unclear.

### 4.2.1 Lack of velocity gradient

In principle, we might expect the observed clumps to be made up of collections of smaller, dense molecular clouds that, once formed (or detached from the uplifted gas), would fall under gravity toward the BCG. Their high density and small cross-section would mean that they would not be significantly slowed by the ram pressure of the surrounding ICM, and would therefore fall ballistically. The free-fall time from their current positions to the BCG nucleus is in the range  $\sim 30\text{--}90 \text{ Myr}$ , while the time required for them to fall from the tips of the lobes to their current locations would be  $\sim 50\text{--}100 \text{ Myr}$ . The high end of these ranges is somewhat smaller than the time-scale on which the jets are thought to have shut down,  $120\text{--}160 \text{ Myr}$ , and we might expect molecular gas to have begun forming earlier, or if

uplifted to have detached and started to fall back earlier, while the jets were still active.

However, there is evidence that the molecular clouds may be somehow supported by the surrounding medium. Olivares et al. (2019) and Russell et al. (2019) point out that where gradients are seen in molecular filaments they are generally weak, inconsistent with the idea that the gas is in free fall. Instead they appear more consistent with gas caught in the stream lines behind rising radio lobes, with gas either being drawn outward or beginning to fall back toward the BCG. Previous studies have shown that even where gradients are measured (e.g. Russell et al. 2016, 2017b; Vantyghem et al. 2016, 2018) their inclinations would all appear to be close to the plane of the sky if the filaments were assumed to be in free fall. While any individual system could be aligned so as to present only a small line-of-sight velocity gradient, this cannot be the case for all clusters. Olivares et al. (2019) conclude that the molecular gas infall velocities must be inherently small. It therefore seems likely that the molecular gas retains some connection with its surroundings and is slowed by drag forces, perhaps associated with enveloping layers of warmer ionized gas (Li et al. 2018), or arising from the magnetic field of the ICM (McCourt et al. 2015). This would allow for material to be uplifted behind rising lobes, as well as slowing its eventual fall back toward the BCG.

Considering IRAS 09104+4109 alone, we are limited in what we can say about the velocity structure of the clouds. The velocities determined from spectral fitting of the clouds along the jets are all consistent within uncertainties. The smoothed velocity map shows only small differences, and on the north side of the BCG we only see clump N2, so we cannot say whether there might be any gradient between that clump and clump C. The lack of any gradient may mean that the CO is oriented close to the plane of the sky, but as any gradients are probably inherently small, we cannot place strong limits on orientation. Deeper, higher resolution observations might provide a clearer picture of the velocity structure and the kinematic state of the molecular gas.

#### 4.2.2 The optical filaments as a locus of cooling

One difference between IRAS 09104+4109 and other systems is that we do not see a clear correlation between the molecular gas and the optical filaments. There is a suggestion of correlation between clump C and the inner filament, but no indications of optical filaments at the positions of the smaller clumps, or along the radio jets in general. One reason for this is probably the lack of deep H $\alpha$  imaging; owing to the redshift of the cluster, the *HST* observations used either broad-band filters or a narrow filter chosen to target [O III], which is significantly weaker line. We may therefore simply be missing a significant fraction of the ionized gas emission. Another possibility is that the detected filaments are illuminated by emission from the AGN, and that other filaments that lie outside the opening angle of its ionization cones are not intrinsically luminous enough to be detected. Since the radio jets and ionization cones are not well aligned (as we will discuss in Section 4.3), this could explain why we do not observe the expected filaments along the jets. Lastly, it should be noted that if a very extended diffuse CO component is present, and overlaps the detected optical filaments, NOEMA may resolve it out or be insensitive to it. However, we would normally expect the molecular gas to be found preferentially in bright ionized gas filaments, so this does not explain why no filaments are seen at the position of the outer CO clumps.

The position of clump C on one side of the BCG may indicate that the inner optical filament and bright X-ray excess north-west of the

BCG nucleus are sites of rapid cooling from the ICM. Crawford & Vanderriest (1996) showed that the nebular emission in the inner optical filament has a velocity  $< 100 \text{ km s}^{-1}$  offset from the nucleus, and a velocity dispersion of  $\sim 250\text{--}400 \text{ km s}^{-1}$ . This agrees fairly well with our modelling of the dominant line component in clump C ( $\langle v \rangle \sim 70 \text{ km s}^{-1}$ , FWHM  $\sim 260 \text{ km s}^{-1}$ ). This supports the idea that the two gas phases have a common origin. The negative velocity tail in the spectrum of clump C suggests there is a component of the gas with a broader velocity dispersion, perhaps indicating a different origin. Alternatively this might represent material that is moving from clump C deeper into the BCG potential well, gaining velocity as it falls.

#### 4.2.3 External origin via a gas-rich merger

Thus far we have discussed the molecular gas in terms of cooling from the ICM. We can also consider the possibility that cool gas has been brought into the BCG via a galaxy merger or interaction. OS12 showed the cluster to be sloshing, probably indicating a recent minor merger or flyby encounter with a group-mass object. They hypothesized that such a merger might have brought a large, gas-rich galaxy into the cluster core. However, in a massive cluster such as CL 09104+4109 ram-pressure stripping is quite effective at removing gas from infalling galaxies. Only galaxies on relatively radial orbits are likely to reach the region around the BCG while retaining a significant cool gas reservoir. Galaxies on more circular orbits will take many orbital periods to lose energy through dynamical friction, and their long exposure to ram pressure seems like to leave them denuded of gas by the time they reach the cluster core. The mass of the cluster ( $M_{200} \sim 8 \times 10^{14} M_{\odot}$ ; OS12) suggests a velocity dispersion for the galaxy population of  $\sim 1000 \text{ km s}^{-1}$ . This is comparable to the sound speed of the ICM in the cluster core, which has a temperature  $\leq 4 \text{ keV}$  within  $\sim 50 \text{ kpc}$ . We can expect galaxies on radial orbits to be moving at velocities considerably greater than the cluster velocity dispersion at their closest approach to the BCG, and they would thus be supersonic in the ICM. Examination of populations of jellyfish galaxies in clusters supports these expectations. These galaxies are found to be predominantly recently accreted by the cluster, usually on radial orbits, moving with systematically higher absolute line-of-sight velocities than the general galaxy population (Jaff   et al. 2018). Stripping occurs preferentially in the dense ICM of cluster cores, but in these regions the galaxy velocities reach their peak, so the velocity of captured gas relative to the BCG would need to be greatly reduced to bring it down to the low values we see in clump C. Achieving all of this without destroying the molecular gas through heating and cloud disruption seems unlikely.

#### 4.3 Orientation of the AGN and jet axis

The roughly equal length and brightness of the large-scale radio jets and lobes suggests that they are aligned relatively close to the plane of the sky (Hines & Wills 1993; Hines et al. 1999) or at least not close to the line of sight. As discussed above, the lack of a velocity gradient in the CO along the jets is not a strong constraint, but it is at least consistent with a jet alignment close to the plane of the sky.

The orientation of the central engine of IRAS 09104+4109 has been the subject of much discussion, using detailed multiwavelength modelling to try to estimate the opening angle and angle with respect to the line of sight of the torus. Hines & Wills (1993) first noted that the old radio jets fall outside the opening angle of the AGN ionization cones. Based on the corrected polarized flux observed from the QSO ionization cones, the AGN torus is aligned such that its opening has a



projected PA of  $98^\circ$  (from west; Hines et al. 1999), whereas the axis of the radio jets has PA =  $63^\circ$ . The most recent modelling, combining infrared and X-ray constraints, suggests that the AGN is tilted  $\sim 35^\circ$  toward the line of sight with a half-opening angle also  $\sim 35^\circ$ . If the jet axis is in the plane of the sky, the angle between the axis of the jets and the current AGN alignment would therefore be  $\sim 45^\circ$ – $50^\circ$ . This places the jets outside the current opening angle.

This suggests that, as well as changing from a radio galaxy to a QSO over the past 120–160 Myr, the AGN has also undergone a change in its axis. This could be achieved through the merger of a comparable mass supermassive black hole (SMBH). This would imply a major galaxy merger in the recent past of IRAS 09104+4109. Whether the traces of such a merger would be obvious in the available *HST* data is unclear. A more likely alternative is that the accretion disc of the QSO was initially misaligned with its rotation axis, causing a realignment of the SMBH. Babul, Sharma & Reynolds (2013) discuss the conditions necessary for such a realignment, finding that it is most likely to occur when the accretion rate is high (implying a thin disc and quasar-mode AGN) and SMBH spin relatively low. The SMBH mass estimate of Kong & Ho (2018),  $M_{\text{SMBH}} = 2.3^{+10.0}_{-1.9} \times 10^8 M_\odot$ , has large uncertainties, but adopting it and (conservatively) assuming that the SMBH axis has changed by  $35^\circ$ , we can estimate the mass of gas that would need to have been accreted via the thin disc (equation 12 of Babul et al. 2013) to be  $M_{\text{gas}} = 2.3^{+9.5}_{-1.9} \times 10^6 M_\odot$ . This is a small fraction of the current molecular gas reservoir.

If we assume that the radiative age of the radio jets (120–160 Myr) is a good estimate of the time at which the accretion rate rose and the AGN entered its current QSO state, then the implied accretion rate is only  $\sim 0.02 M_\odot \text{ yr}^{-1}$ . However, the likely accretion rate over that time is higher. The only evidence of jet activity since the old jets shut down is the 200 pc scale VLBA-detected radio double in the BCG core, so we must assume that the AGN has been a high accretion rate QSO for most of the last  $10^8$  yr. This implies an accretion rate of at least 1 per cent of the Eddington rate,  $\sim 0.05 M_\odot \text{ yr}^{-1}$ . It is thus likely that the SMBH has accreted at least  $6 \times 10^6 M_\odot$  over the past 120 Myr, roughly 2.5 per cent of its current mass, but only 0.01 per cent of the available molecular gas reservoir. Clearly this reservoir is quite sufficient to fuel the QSO, even at much higher accretion rates, for long periods (providing the gas reaches the central engine) and to drive the apparent change in its axis.

#### 4.4 Star formation

Bildfell et al. (2008) found blue colours in the stellar population of IRAS 09104+4109 extending out to  $\sim 20$  kpc. However, this does not mean that the current burst of star formation (SF) extends throughout the galaxy. The blue optical colours likely represent a small mass of young stars formed during the earlier burst of SF that occurred 70–200 Myr ago. Following OS12, we can estimate the size of star-forming disc that we would expect given the measured SFR, assuming it follows the standard Kennicutt–Schmidt relation (Kennicutt 1998),

$$\text{SFR} = 0.017 \times M_{\text{gas}} v_c / R, \quad (3)$$

where  $M_{\text{gas}}$  is the mass of gas available to fuel SF,  $v_c$  is the rotation velocity of the disc, and  $R$  is the disc radius. We adopt  $\text{SFR} = 110 M_\odot \text{ yr}^{-1}$  (Farrah et al. 2016), and  $v_c = 200 \text{ km s}^{-1}$  based on the [O III] velocity profile of Crawford & Vanderriest (1996). If we consider the whole of clump C ( $2.62 \times 10^{10} M_\odot$ ) as available to fuel SF, this would imply a disc of radius  $\sim 830$  pc ( $\sim 0.15$  arcsec). More conservatively, if we assume only the negative velocity component of clump C, which is centred closer to the BCG core, and adopt a value

of  $\alpha_{\text{CO}} = 0.8$  (more appropriate for this HyLIRG), the radius may be as low as  $\sim 45$  pc ( $\sim 0.008$  arcsec). As noted by OS12, a compact, dense, gas-rich star-forming disc around the AGN provides a natural explanation for the heavy obscuration of the source seen in X-ray and infrared–near-ultraviolet spectral energy distribution (SED) fitting. Farrah et al. (2016) argue, based on their combined SED and X-ray spectral modelling, that the vertical height of the obscurer is likely  $\sim 20$  pc, and its outer edge likely within 125 pc. This is at least comparable to the lower end of the range we estimate for the star-forming disc.

An example of a star-forming disc of similar size in a BCG with a filamentary nebula can be found in NGC 1275. Observations of molecular gas have confirmed the presence of a 50–100 pc rotating molecular disc (Scharwächter et al. 2013; Nagai et al. 2019) around the AGN. VLBA observations revealed a roughly circular  $\sim 70$  kpc radius region of radio continuum emission around the AGN that was initially interpreted as a minihalo (Silver, Taylor & Vermeulen 1998) but may in fact represent SF within the molecular disc (Nagai & Kawakatu 2021). IRAS 09104+4109 would therefore not be unique if it hosts such a disc.

#### 4.5 High-velocity CO component

The high-velocity CO component is only marginally detected, but potentially interesting if its existence can be confirmed. Its origin is unclear. The clumps are  $\sim 20$  kpc from the AGN, a comparable scale to the largest molecular gas outflows observed around quasars, as discussed in Section 4.2. However, given what we know about the alignment of the AGN, it seems very unlikely that two clumps, on either side of the AGN, would both have such similar blueshifted velocities; we would expect a velocity gradient across the core. It should also be noted that the two clumps have an alignment similar to the old radio jets, not the ionization cones of the QSO, as would be expected if they had been expelled from the BCG by a radiation-driven wind. The X-ray observations also provide strong evidence against an outflow on this scale. OS12 were able to trace the X-ray surface brightness and temperature profiles on scales smaller than the high-velocity clumps and saw no evidence of such disturbance. An outflow, even on this smaller scale, seems unlikely.

Another possibility is that the molecular gas is the remnant of an infalling galaxy. Molecular line observations of ‘jellyfish’ galaxies, cold-gas-rich spirals being ram-pressure stripped as they fall into clusters, have shown that molecular gas can be stripped from the disc, and survive transport several tens of kpc (e.g. Jáchym et al. 2014, 2017, 2019). We see no clear corresponding galaxy for the gas to have been stripped from, but a galaxy tidally disrupted by a passage close to the BCG might not be obvious in the available data. However, the remaining ionized gas in the stripped galaxy should be more easily detectable. No such components are visible in the *HST* optical images at or near the location of the CO clumps. Deeper CO observations would be needed to confirm their existence.

#### 5 SUMMARY AND CONCLUSIONS

IRAS 09104+4109 is a rare, relatively low-redshift example of a class of system believed to be common at earlier epochs: a QSO at the centre of a cooling flow galaxy cluster. Prior observations have shown that the HyLIRG BCG hosts a type 2 (obscured) QSO, as well as an ongoing,  $< 50$  Myr old starburst. A 70–200 Myr old stellar population component indicates a previous burst of SF, while  $\sim 70$  kpc long radio jets, with a spectral age of 120–160 Myr, suggest that the AGN may have shifted from a radiatively inefficient

jet-dominated mode to its current radiatively efficient activity in the recent past. The fuelling of such a system, and its impact on the surrounding cluster, is relevant to the question of how high-redshift QSOs can maintain the thermal balance of the ICM. We therefore observed IRAS 09104+4109 with the NOEMA interferometer and JCMT SCUBA-2 instrument, to investigate its molecular gas and dust content. Our conclusions are summarized below.

(i) As in many cool-core clusters with central FR-I radio galaxies, the CO(2–1) maps show that the molecular gas is primarily located in a series of clumps extending along the path of the rise of the old radio lobes, with a total mass of  $\sim 4.5 \times 10^{10} M_{\odot}$  (for  $\alpha_{\text{CO}} = 4.6$ , or  $\sim 7.9 \times 10^9 M_{\odot}$  for  $\alpha_{\text{CO}} = 0.8$ ). The velocities of these clumps are within  $100 \text{ km s}^{-1}$  of the recession velocity of the BCG, and there is no evidence of any significant velocity gradient along the jets. Roughly 55 per cent of the gas is located in a central clump on the north-east side of the BCG, coincident with the base of the brightest of the optical filaments and with a bright spur in the X-ray residual map. This suggests that this may be a region of rapid cooling from the ICM. The molecular clumps are observed out to  $\sim 55 \text{ kpc}$  from the nucleus. This is exceptional; molecular gas filaments in low-redshift clusters are not generally observed to extend beyond  $25 \text{ kpc}$ . The velocity dispersion of the molecular gas clumps is relatively low ( $\sim 280\text{--}320 \text{ km s}^{-1}$ ) except in the central clump, where a broader tail at low velocities is observed. Comparison with the archival IRAM 30-m spectrum suggests that the NOEMA data have captured all the emission from the region covered by the 30-m beam, with additional emission coming from clumps at greater distances along the jets.

(ii) Based on the available profiles of ICM properties from OS12, we find that the molecular gas is contained within a region where the ratio of the azimuthally averaged isochoric cooling time to the free-fall time is  $t_{\text{cool}}/t_{\text{ff}} \lesssim 25$ , and the ratio of cooling time to eddy turnover time is likely  $t_{\text{cool}}/t_{\text{eddy}} \sim 1$ . We find that cavities associated with the jets and lobes are in principle capable of uplifting a mass of gas comparable to the molecular gas mass we observe. However, when we consider the additional mass of warmer material in which the molecular gas must be embedded, or from which it condensed, this possibility looks less likely. It should also be noted that while the *Chandra* observation detected relatively large cavities correlated with the jets, it lacked the necessary depth to confirm the presence of cavities associated with the lobes. It seems more plausible that the molecular gas may have formed *in situ*, from thermally unstable gas that was disturbed by the expansion of the jets, provided sufficient dust survives in these regions to catalyze the formation of molecular gas. An unusual feature is the lack of correlation between the molecular and ionized gas, outside the central clump. This may indicate that only the very brightest nebular emission was detected in previous *HST* observations, or perhaps only those filaments illuminated by the QSO.

(iii) We find a tentative detection of additional CO(2–1) emission at a relative velocity of  $\sim -1450 \text{ km s}^{-1}$ , located in clumps  $\sim 3 \text{ arcsec}/16.5 \text{ kpc}$  north-west and south-east of the nucleus. We briefly consider whether these could be evidence of an outflow driven by the QSO, or a remnant of an infalling, ram-pressure stripped galaxy, but conclude that deeper observations are needed, both to confirm the existence of the clumps and to shed light on their origin.

(iv) We measure the continuum emission of the BCG at  $159.9 \text{ GHz}$  with NOEMA and at  $850 \mu\text{m}$  with SCUBA-2. These two fluxes extend the range of the previously measured far-infrared peak associated with reprocessed emission from the AGN and dusty starburst, but have fluxes well above what would be expected from previous modelling. We model the  $3.6 \mu\text{m}\text{--}1 \text{ m}$  spectrum, and find

that the observed fluxes likely include contributions from nebular free–free emission arising from the ongoing SF in the galaxy. Our modelling suggests a starburst age of  $25 \pm 13 \text{ Myr}$ , consistent with the previous upper limit of  $<50 \text{ Myr}$ . We also find that the spectral index of the power-law emission from the radio jets is  $\alpha = 1.35 \pm 0.06$ , somewhat steeper than previously thought.

Based on the X-ray and radio observations of IRAS 09104+4109, OS12 left open the question of whether its ionized gas filaments were the product of cooling from the ICM or the infall and merger of a gas-rich galaxy, though the latter seemed the less likely option. Our NOEMA observations make clear that ICM cooling has produced a large reservoir of molecular gas in the cluster core, with similar characteristics to those seen in other cool-core clusters. The amount of molecular gas in or near the BCG is certainly sufficient to have fuelled the increase in accretion rate that caused the AGN to change from an FR-I radio galaxy to a QSO, and to have caused the realignment of the AGN axis. The extent of the molecular gas is unusually large, and the mismatch between the molecular and ionized gas is surprising. Further observations of the warm ionized component would be useful to investigate this lack of correlation, and determine whether previous observations were simply too shallow. Deeper observations of the molecular gas and hot ICM would also be beneficial. With the former, we could explore whether the various CO clumps are actually linked by lower density material, determine whether the molecular gas distribution in the BCG is really as asymmetric as it appears, and investigate the  $-1450 \text{ km s}^{-1}$  component. Deeper X-ray observations with *Chandra* have recently been approved, and should allow us to determine the size of any cavities associated with the radio lobes, and thus measure their uplift capacity, as well as investigating the ICM conditions in the bright spur that overlaps clump C, apparently the most rapidly cooling region in this unique system.

## ACKNOWLEDGEMENTS

We thank the anonymous referee for comments that materially improved the paper. EO'S gratefully acknowledges the support for this work provided by the National Aeronautics and Space Administration (NASA) through *Chandra* Award Number GO0-21112X issued by the *Chandra* X-ray Center, which is operated by the Smithsonian Astrophysical Observatory for and on behalf of the National Aeronautics and Space Administration under contract NAS8-03060. AB acknowledges research support from the Natural Sciences and Engineering Research Council of Canada (NSERC). This work is based on observations carried out under project number W18DB with the IRAM NOEMA Interferometer. IRAM is supported by INSU/CNRS (France), MPG (Germany), and IGN (Spain). The James Clerk Maxwell Telescope is operated by the East Asian Observatory on behalf of The National Astronomical Observatory of Japan, Academia Sinica Institute of Astronomy and Astrophysics, the Korea Astronomy and Space Science Institute, and Center for Astronomical Mega-Science (as well as the National Key R&D Program of China with no. 2017YFA0402700). Additional funding support is provided by the Science and Technology Facilities Council of the United Kingdom and participating universities in the United Kingdom and Canada. Additional funds for the construction of SCUBA-2 were provided by the Canada Foundation for Innovation.

## DATA AVAILABILITY

The NOEMA data used in this work, program W18DB, are available from the IRAM Science Data Archive upon request. The JCMT

SCUBA-2 data, programs M18BP056, M15BL114, and M12AC15, are available in the JCMT Science Archive at the Canadian Astronomy Data Centre, <http://www.cadc-ccda.hia-ih.nrc-cnrc.gc.ca/en/jcmt/>.

## REFERENCES

- Aravena M., Wagg J., Papadopoulos P. P., Feain I. J., 2011, *ApJ*, 737, 64
- Babul A., Sharma P., Reynolds C. S., 2013, *ApJ*, 768, 11
- Babyk I. V., McNamara B. R., Tamhane P. D., Nulsen P. E. J., Russell H. R., Edge A. C., 2019, *ApJ*, 887, 149
- Bildfell C., Hoekstra H., Babul A., Mahdavi A., 2008, *MNRAS*, 389, 1637
- Bischetti M. et al., 2019, *A&A*, 628, A118
- Boquien M., Burgarella D., Roehlly Y., Buat V., Ciesla L., Corre D., Inoue A. K., Salas H., 2019, *A&A*, 622, A103
- Bruzual G., Charlot S., 2003, *MNRAS*, 344, 1000
- Canning R. E. A. et al., 2014, *MNRAS*, 444, 336
- Cavagnolo K. W., Donahue M., Voit G. M., Sun M., 2008, *ApJ*, 683, L107
- Cavagnolo K. W., McNamara B. R., Nulsen P. E. J., Carilli C. L., Jones C., Birzan L., 2010, *ApJ*, 720, 1066
- Chabrier G., 2003, *ApJ*, 586, L133
- Chapin E. L., Berry D. S., Gibb A. G., Jenness T., Scott D., Tilanus R. P. J., Economou F., Holland W. S., 2013, *MNRAS*, 430, 2545
- Chartas G. et al., 2020, *MNRAS*, 496, 598
- Cicone C. et al., 2014, *A&A*, 562, A21
- Cicone C. et al., 2015, *A&A*, 574, A14
- Combes F., García-Burillo S., Braine J., Schinnerer E., Walter F., Colina L., 2011, *A&A*, 528, A124
- Conselice C. J., Gallagher J. S., III, Wyse R. F. G., 2001, *AJ*, 122, 2281
- Crawford C. S., Vanderriest C., 1996, *MNRAS*, 283, 1003
- Crawford C. S., Sanders J. S., Fabian A. C., 2005a, *MNRAS*, 361, 17
- Crawford C. S., Hatch N. A., Fabian A. C., Sanders J. S., 2005b, *MNRAS*, 363, 216
- Dale D. A., Helou G., Magdis G. E., Armus L., Díaz-Santos T., Shi Y., 2014, *ApJ*, 784, 83
- Dame T. M., 2011, preprint ([arXiv:1101.1499](https://arxiv.org/abs/1101.1499))
- Dempsey J. T. et al., 2012, in Holland W. S., ed., Proc. SPIE Vol. 8452, Millimeter, Submillimeter, and Far-Infrared Detectors and Instrumentation for Astronomy VI, SPIE, Bellingham, p. 845202
- Dempsey J. T. et al., 2013, *MNRAS*, 430, 2534
- Downes D., Solomon P. M., 1998, *ApJ*, 507, 615
- Efstathiou A., Rowan-Robinson M., 1995, *MNRAS*, 273, 649
- Efstathiou A., Rowan-Robinson M., Siebenmorgen R., 2000, *MNRAS*, 313, 734
- Efstathiou A., Christopher N., Verma A., Siebenmorgen R., 2013, *MNRAS*, 436, 1873
- Fabian A. C., 2012, *ARA&A*, 50, 455
- Fabian A. C., Sanders J. S., Allen S. W., Crawford C. S., Iwasawa K., Johnstone R. M., Schmidt R. W., Taylor G. B., 2003, *MNRAS*, 344, L43
- Farrah D. et al., 2016, *ApJ*, 831, 76
- Ferland G. J., Korista K. T., Verner D. A., Ferguson J. W., Kingdon J. B., Verner E. M., 1998, *PASP*, 110, 761
- Fluetsch A. et al., 2019, *MNRAS*, 483, 4586
- Fogarty K. et al., 2019, *ApJ*, 879, 103
- Gaspari M., Melioli C., Brighenti F., D'Ercole A., 2011, *MNRAS*, 411, 349
- Gaspari M., Ruszkowski M., Sharma P., 2012, *ApJ*, 746, 94
- Gaspari M., Ruszkowski M., Oh S. P., 2013, *MNRAS*, 432, 3401
- Gaspari M. et al., 2018, *ApJ*, 854, 167
- Gendron-Marsolais M. et al., 2018, *MNRAS*, 479, L28
- Gildas Team, 2013, Astrophysics Source Code Library, record ascl:1305.010
- Gitti M., Brighenti F., McNamara B. R., 2012, *Adv. Astron.*, 2012, 950641
- Gould R. J., Salpeter E. E., 1963, *ApJ*, 138, 393
- Guillard P., Boulanger F., Pineau des Forets G., Appleton P. N., 2009, *A&A*, 502, 515
- Hines D. C., Wills B. J., 1993, *ApJ*, 415, 82
- Hines D. C., Schmidt G. D., Wills B. J., Smith P. S., Sowinski L. G., 1999, *ApJ*, 512, 145
- Hlavacek-Larrondo J., Fabian A. C., Edge A. C., Ebeling H., Allen S. W., Sanders J. S., Taylor G. B., 2013, *MNRAS*, 431, 1638
- Hogan M. T. et al., 2017, *ApJ*, 851, 66
- Hollenbach D., Salpeter E. E., 1971, *ApJ*, 163, 155
- Inoue A. K., 2011, *Earth Planets Space*, 63, 1027
- Jáchym P., Combes F., Cortese L., Sun M., Kenney J. D. P., 2014, *ApJ*, 792, 11
- Jáchym P. et al., 2017, *ApJ*, 839, 114
- Jáchym P. et al., 2019, *ApJ*, 883, 145
- Jaffé Y. L. et al., 2018, *MNRAS*, 476, 4753
- Jenness T., Chapin E. L., Berry D. S., Gibb A. G., Tilanus R. P. J., Balfour J., Tilanus V., Currie M. J., 2013, Astrophysics Source Code Library, record ascl:1310.007
- Kackley R., Scott D., Chapin E., Friberg P., 2010, in Radziwiłł N. M., Bridger A., eds, Proc. SPIE Vol. 7740, Software and Cyberinfrastructure for Astronomy. SPIE, Bellingham, p. 77401Z
- Kennicutt R. C., Jr, 1998, *ApJ*, 498, 541
- Kleinmann S. G., Hamilton D., Keel W. C., Wynn-Williams C. G., Eales S. A., Becklin E. E., Kuntz K. D., 1988, *ApJ*, 328, 161
- Kong M., Ho L. C., 2018, *ApJ*, 859, 116
- Koprowski M., 2015, PhD thesis, Univ. Edinburgh
- Lakhchaura K. et al., 2018, *MNRAS*, 481, 4472
- Li Y., Bryan G. L., 2014a, *ApJ*, 789, 54
- Li Y., Bryan G. L., 2014b, *ApJ*, 789, 153
- Li Y., Bryan G. L., Ruszkowski M., Voit G. M., O'Shea B. W., Donahue M., 2015, *ApJ*, 811, 73
- Li Y., Ruszkowski M., Tremblay G., 2018, *ApJ*, 854, 91
- McCourt M., Sharma P., Quataert E., Parrish I. J., 2012, *MNRAS*, 419, 3319
- McCourt M., O'Leary R. M., Madigan A.-M., Quataert E., 2015, *MNRAS*, 449, 2
- McDonald M., Veilleux S., Rupke D. S. N., Mushotzky R., 2010, *ApJ*, 721, 1262
- McDonald M., Veilleux S., Mushotzky R., 2011, *ApJ*, 731, 33
- McDonald M. et al., 2015, *ApJ*, 811, 111
- McDonald M. et al., 2019, *ApJ*, 885, 63
- McNamara B. R., Nulsen P. E. J., 2007, *ARA&A*, 45, 117
- McNamara B. R., Russell H. R., Nulsen P. E. J., Hogan M. T., Fabian A. C., Pulido F., Edge A. C., 2016, *ApJ*, 830, 79
- Nagai H., Kawakatu N., 2021, *ApJ*, 914, L11
- Nagai H. et al., 2019, *ApJ*, 883, 193
- Olivares V. et al., 2019, *A&A*, 631, A22
- O'Sullivan E., Giacintucci S., Vrtilek J. M., Raychaudhury S., David L. P., 2009, *ApJ*, 701, 1560
- O'Sullivan E. et al., 2012, *MNRAS*, 424, 2971 (OS12)
- O'Sullivan E., Kolokythas K., Kantharia N. G., Raychaudhury S., David L. P., Vrtilek J. M., 2018, *MNRAS*, 473, 5248
- Pety J., 2005, in Casoli F., Contini T., Hameury J. M., Pagani L., eds, SF2A-2005: Semaine de l'Astrophysique Française. EDP Sciences, Les Ulis, France, p. 721
- Pipino A., Kaviraj S., Bildfell C., Babul A., Hoekstra H., Silk J., 2009, *MNRAS*, 395, 462
- Pope E. C. D., Babul A., Pavlovski G., Bower R. G., Dotter A., 2010, *MNRAS*, 406, 2023
- Prasad D., Sharma P., Babul A., 2015, *ApJ*, 811, 108
- Prasad D., Sharma P., Babul A., 2017, *MNRAS*, 471, 1531
- Prasad D., Sharma P., Babul A., 2018, *ApJ*, 863, 62
- Prasad D., Sharma P., Babul A., Voit G. M., O'Shea B. W., 2020, *MNRAS*, 495, 594
- Qiu Y., Bogdanović T., Li Y., McDonald M., McNamara B. R., 2020, *Nat. Astron.*, 4, 900
- Rafferty D. A., McNamara B. R., Nulsen P. E. J., 2008, *ApJ*, 687, 899
- Revaz Y., Combes F., Salomé P., 2008, *A&A*, 477, L33
- Reynolds C. S., Lohfink A. M., Babul A., Fabian A. C., Hlavacek-Larrondo J., Russell H. R., Walker S. A., 2014, *ApJ*, 792, L41
- Russell H. R., Fabian A. C., Sanders J. S., Johnstone R. M., Blundell K. M., Brandt W. N., Crawford C. S., 2010, *MNRAS*, 402, 1561

- Russell H. R. et al., 2016, *MNRAS*, 458, 3134  
 Russell H. R. et al., 2017a, *MNRAS*, 472, 4024  
 Russell H. R. et al., 2017b, *ApJ*, 836, 130  
 Russell H. R. et al., 2019, *MNRAS*, 490, 3025  
 Salomé P. et al., 2006, *A&A*, 454, 437  
 Salomé P., Combes F., Revaz Y., Downes D., Edge A. C., Fabian A. C., 2011, *A&A*, 531, A85  
 Scharwächter J., McGregor P. J., Dopita M. A., Beck T. L., 2013, *MNRAS*, 429, 2315  
 Sharma P., McCourt M., Quataert E., Parrish I. J., 2012, *MNRAS*, 420, 3174  
 Silver C. S., Taylor G. B., Vermeulen R. C., 1998, *ApJ*, 502, 229  
 Solomon P. M., Vanden Bout P. A., 2005, *ARA&A*, 43, 677  
 Stalevski M., Ricci C., Ueda Y., Lira P., Fritz J., Baes M., 2016, *MNRAS*, 458, 2288  
 Sulentic J. W., Rosado M., Dultzin-Hacyan D., Verdes-Montenegro L., Trinchieri G., Xu C., Pietsch W., 2001, *AJ*, 122, 2993  
 Temi P., Amblard A., Gitti M., Brighenti F., Gaspari M., Mathews W. G., David L., 2018, *ApJ*, 858, 17  
 Tran H. D., Cohen M. H., Villar-Martin M., 2000, *AJ*, 120, 562  
 Vantyghem A. N. et al., 2016, *ApJ*, 832, 148  
 Vantyghem A. N. et al., 2017, *ApJ*, 848, 101  
 Vantyghem A. N. et al., 2018, *ApJ*, 863, 193  
 Voit G. M., Meece G., Li Y., O’Shea B. W., Bryan G. L., Donahue M., 2017, *ApJ*, 845, 80  
 Voit G. M., Ma C. P., Greene J., Goulding A., Pandya V., Donahue M., Sun M., 2018, *ApJ*, 853, 78  
 Walker S. A., Fabian A. C., Russell H. R., Sanders J. S., 2014, *MNRAS*, 442, 2809  
 Werner N. et al., 2014, *MNRAS*, 439, 2291  
 Wrobel J. M., Walker R. C., Benson J. M., Beasley A., 2000, Strategies for Phase Referencing with the VLBA (VLBA Sci. Memo. 24). Technical Report, NRAO, Socorro



## APPENDIX A: NOEMA CHANNEL MAPS

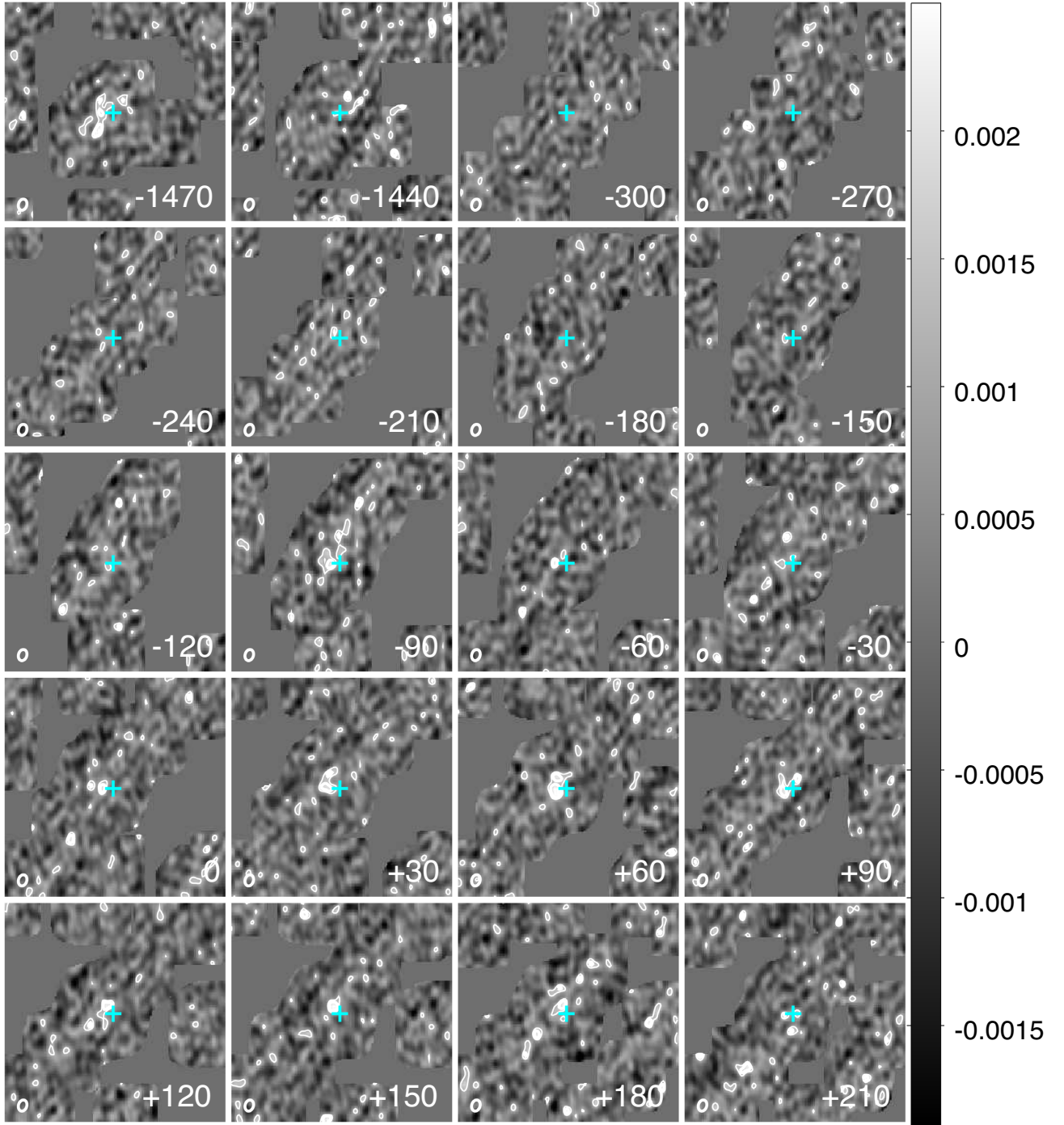


**Figure A1.** Maps of the  $30 \text{ km s}^{-1}$  NOEMA channels used in creating the images in Fig. 1. Solid grey areas are masked as described in Section 3.1. On each panel, heavy and narrow contours mark the  $3\sigma$  and  $2\sigma$  significant regions. The velocity of each channel in  $\text{km s}^{-1}$  is shown in the bottom right of each panel, the beam size by a dashed ellipse in the bottom left, and the position of the AGN by a cyan cross. All panels share the same orientation and scale as in Fig. 1. The colour bar indicates flux density in  $\text{Jy km s}^{-1} \text{ beam}^{-1}$ .

This paper has been typeset from a  $\text{\LaTeX}$  file prepared by the author.